An Electromagnetic Vorticity and Velocity Sensor for Observing Finescale Kinetic Fluctuations in the Ocean

THOMAS B. SANFORD,* JAMES A. CARLSON,+ JOHN H. DUNLAP, MARK D. PRATER,# AND REN-CHIEH LIEN

Applied Physics Laboratory, University of Washington, Seattle, Washington

(Manuscript received 4 August 1997, in final form 18 September 1998)

ABSTRACT

An instrument has been developed that measures finescale velocity and vorticity in seawater based on the principles of motional induction. This instrument, the electromagnetic vorticity meter (EMVM), measures components of the gradient and Laplacian of the electrostatic potential field induced by the motion of seawater through an applied magnetic field. The principal innovation described here is the development of a sensor for measuring small-scale vorticity. The sensor head consists of a strong NdFeB magnet, a five-electrode array, low-noise preamplifiers, and 20-Hz digitizers. The main electronics includes attitude sensors, batteries, a microprocessor, and a hard disk. The vorticity sensors are usually carried on a heavy towed vehicle capable of vertically profiling to 200 m and at tow speeds of several knots.

The theoretical response functions of the EMVM are evaluated for velocity and vorticity. Extensive measurements were obtained in Pickering Passage, Washington, as the sensor vertically profiled in an unstratified tidal channel. During periods of strong flow, the vertical structure of all properties confirmed expectations for a fully developed turbulent bottom boundary layer. EMVM observations of velocity and vorticity are shown to be in agreement with the theoretical response function for isotropic turbulence. A principal result is that the vertical flux of spanwise vorticity (i.e., $\overline{w'\omega_y'}$) is positive (i.e., flux is away from seabed) and vertically uniform. The vertical eddy diffusivity for vorticity is about 5×10^{-2} m^2 s^{-1}, which is about the same value as for momentum.

1. Introduction

Vorticity is fundamentally important in fluid mechanics and small-scale physical oceanography. Few processes generate or dissipate it, and once there, it can be long lived. In fact, some theories treat vorticity as a conserved quantity that does not change as the fluid moves. Often the description of a particular flow feature is most simply stated in terms of the vorticity distribution and dynamics. The vorticity ($\boldsymbol{\omega}$) of a velocity field ($\mathbf{v}$) is defined as

$$\boldsymbol{\omega} = \boldsymbol{\nabla} \times \mathbf{v}. \tag{1}$$

The role of vorticity is clearly revealed in an alternative formulation of the Navier–Stokes equations for homogeneous fluid motion:

$$\partial \mathbf{u}/\partial t + \boldsymbol{\nabla}\left(\frac{1}{2}\mathbf{u}\cdot\mathbf{u} + \frac{p}{\rho} + gz\right) = -\boldsymbol{\omega} \times \mathbf{u} - \nu\boldsymbol{\nabla} \times \boldsymbol{\omega}, \tag{2}$$

where $\mathbf{u}$ is velocity, ρ is density, p is pressure, g is gravity, z is height, and ν is the molecular viscosity. The first term on the right-hand side of (2) is often called the *vortex force*, and the other term is related to the dissipation rate of kinetic energy. The nonlinear vortex force contributes to the cascade of energy between the large scales of generation and the smaller scales of dissipation.

There are many environmental fluid studies in which vorticity plays vital roles in the dynamics. For example, Müller et al. (1986) state that in order to test recent theories of oceanic fine structure, ''we need to develop techniques to measure potential vorticity on small scales.'' Vortical motion is possibly the explanation behind much of the variability observed in the ocean that cannot be assigned to internal waves. Because the natural background of small-scale vorticity is expected to be small, observations of enhanced levels may indicate the origin or forcing of ocean vorticity. The torque need-

* Additional affiliation: School of Oceanography, University of Washington, Seattle, Washington.
+ Current affiliation: Sea-Bird Electronics, Inc., Bellevue, Washington.
# Current affiliation: Graduate School of Oceanography, University of Rhode Island, Narragansett, Rhode Island.

Corresponding author address: Dr. Thomas B. Sanford, Applied Physics Laboratory, University of Washington, 1013 N.E. 40th St., Seattle, WA 98105.
E-mail: sanford@apl.washington.edu

ed to spin up a vortex about the vertical axis is not easily provided within the upper ocean. Wind stress or water moving past a surface are potential sources, and vorticity is definitely a signature of wave instability and breakdown.

Velocity and vorticity are vitally important to understanding the role of motions at scales of 1–10 m. Gargett et al. (1981) report a change in the slope of vertical shear spectra at about 10-m vertical wavelength. The horizontal wavelengths associated with this spectral ''knee'' are not known. Müller (1984) argues that small-scale vortical structures exist and may be responsible for the noninternal-wave ''fine structure'' invoked to explain moored current and temperature measurements. In addition, Müller makes the point that the vortical mode is needed for a complete description of small-scale motions and for the enstrophy cascade. Lin and Pao (1979) have demonstrated in laboratory experiments that stratification inhibits vertical motion. Thus a stratified fluid quickly exhibits quasi-two-dimensional motion with dominantly vertical vorticity. This indicates an inverse cascade of vorticity variance toward a larger scale.

In spite of the advantages of measuring vorticity directly, few sensors have been developed with that capability at appropriate length scales and with useful accuracy. This is unfortunate because Saffman (1981) claims that ''the invention of an accurate non-intrusive, fine-resolution vorticity meter would be of inestimable value. . . .'' Thwaites et al. (1995) report on a vorticity sensor that measures area-averaged vorticity from acoustic measurements of the velocity integral around a closed path (i.e., circulation). The present paper discusses the development and performance of an electromagnetic vorticity meter (EMVM). The EMVM determines a single component of water vorticity and the two orthogonal velocity components. These flow characteristics are determined from motionally induced voltages as seawater passes over a magnet. Velocity is obtained from the potential gradients within an array of electrodes; vorticity is obtained from the Laplacian of the potential field.

For the EMVM to be scientifically useful, it must have a noise level significantly below the expected ambient level of vorticity in the open ocean. This level can be inferred from estimates of the energy levels of current fine structure. From observations during the Internal Wave Experiment (IWEX), where the presumption of current fine structure was first invoked (Briscoe 1975), the nonlinear contamination is estimated to be about 1 cm s^{-1} rms at high frequency ($\sim$1 cph). A simple model for the relative vorticity of a circular vortex with a peak speed 1.4 cm s^{-1} and a radius L is

$$\zeta = \frac{2 \times 1.4}{L} \times 10^{-2}\ \mathrm{s}^{-1}.$$

The factor of 2 represents the contributions of both velocity components. In IWEX, the coherence at high frequency dropped rapidly at less than 10-m separations, so L must be around 10 m or less and ζ would be about 0.003 s^{-1}.

Another estimate of the anticipated level of vorticity can be formed from kinetic energy dissipation rates, ε. A single component of the 3D turbulent vorticity is equal to $(\varepsilon/3\nu)^{1/2}$. Typical values of ε are 10^{-7} W kg^{-1} in the convective mixed layer and similar magnitude in the wind-driven mixed layer. It is 10^{-6} W kg^{-1} in a tidal channel bottom boundary layer and about 10^{-10} W kg^{-1} in the abyssal ocean. So, the lower bound of the vorticity is about 3×10^{-3} s^{-1}, which is about the same as that for current fine structure. But the lower bound of the vorticity in the surface mixed layer and in a tidal channel is at least one order of magnitude greater. The EMVM has a demonstrated noise level of about 10^{-3} s^{-1}.

This paper describes the principles of operation behind the EMVM, documents its design and construction, and presents some results of its performance in the laboratory and field.

2. Principles of operation

The EMVM operates on the principles of motional induction governing the electric fields induced as seawater moves through a magnetic field. These principles are the basis of the conventional electromagnetic current meter, which generates a magnetic field and measures the potential differences between spaced electrodes. In the EMVM, the first derivatives ($\nabla\phi$) and second derivatives ($\nabla^2\phi$) of the electric potential field (ϕ) are measured. The first differences yield the usual linear velocity components; the second determine a component of water vorticity.

The first mention of measuring $\nabla^2\phi$ to estimate a component of small-scale vorticity appears to be by Grossman et al. (1957). Baker (1971) described the construction and use of a ''vortex probe'' based on the two-dimensional Laplacian of the potential field. Tsinober et al. (1987) described a very small ($\approx$1 mm) probe used to study turbulence in saltwater. They reported good success with the method and offered the following list of advantages.

- It offers the possibility of distinguishing between velocity components because of the vector nature of the basic relation and the sensitivity to the direction of the flow.
- It is linear and does not require any calibration procedure (in fact, no calibration procedure can be applied to this method).
- It is insensitive to the physical properties of the fluid medium.
- It yields an instantaneous measure of quantities fluctuating in time; that is, its response time is extremely small.
- It operates in flows of a complex nature, and it allows

the determination of the separation and reattachment points and the moment and position of the turbulence onset or relaminization.
- It can be used in nonisotropic turbulence for determining the spectral interval where the turbulence becomes locally isotropic by using high-pass filters and checking if the relations between turbulence components are valid.

a. Governing equations

The governing equation for the motionally induced potential differences in seawater is

$$\nabla\phi = \mathbf{v} \times \mathbf{B} - \mathbf{J}/\sigma, \tag{3}$$

where ϕ is the electrostatic potential (V), $\mathbf{v}$ is the water velocity (m s^{-1}), $\mathbf{B}$ is the magnetic field (T), $\mathbf{J}$ is the electric current density (A m^{-2}), and σ is the electrical conductivity (S m^{-1}) of seawater (assumed constant). The EMVM works by measuring the electric field induced by the vorticity of seawater in a magnetic field. Because $\nabla \cdot \mathbf{J} = 0$, the divergence of (3), yields

$$\nabla^2\phi = \nabla \cdot (\mathbf{v} \times \mathbf{B}) = \mathbf{B} \cdot \boldsymbol{\omega} - \mathbf{v} \cdot \nabla \times \mathbf{B}, \tag{4}$$

where $\boldsymbol{\omega}$ is the vorticity (s^{-1}) of the water (i.e., $\nabla \times \mathbf{v}$). The last term in (4) is small compared with the next-to-last term and can be ignored. This may be easily seen by noting that from Ampere's law $\nabla \times \mathbf{B}$ may be replaced by $\mu_0\mathbf{J}$, making the second term of order $\mu_0\sigma v l$ relative to the first term, where μ_0 is the magnetic susceptibility of free space ($4\pi \times 10^{-7}$ Hm^{-1}), and v and l are the velocity and length scales of the vortical motion. The quantity $(\mu_0\sigma)^{-1}$ is the magnetic diffusivity, which is about 2×10^5 m^2 s^{-1} for seawater. The second term does not exceed 10^{-4} of the first for typical turbulent motions on scales of 1–10 m. Thus,

$$\nabla^2\phi = \mathbf{B} \cdot \boldsymbol{\omega}, \tag{5}$$

which is $B_3\omega_3$, where the subscript 3 denotes the component parallel to the magnetic field.

b. Measurement approach

An array of electrodes is used to sense voltages that result from velocity and vorticity in the presence of an applied magnetic field. Each outer electrode (located at x, y, z) is referenced to the center (ground) electrode, and the output of the electronics circuit is the difference in the voltages between the electrode arms.

The potential gradient in the x direction is estimated as

$$\frac{\Delta\phi}{\Delta x} = \frac{\phi(l,0,0) - \phi(0,0,0) - \phi(-l,0,0) + \phi(0,0,0)}{2l} = \frac{\phi(l,\,0,\,0) - \phi(-l,\,0,\,0)}{2l}. \tag{6a}$$

The finite difference approximation of $\partial^2\phi/\partial x^2$ is given by

$$\frac{\Delta^2\phi}{\Delta x^2} = \frac{\phi(l,\,0,\,0) + \phi(-l,\,0,\,0) - 2\phi(0,\,0,\,0)}{l^2}. \tag{6b}$$

This analysis can be extended to the generalized three-dimensional case in which three independent measurements are made and combined to yield a three-dimensional approximation of $\nabla^2\phi$.

It should be emphasized that $\nabla^2\phi$ is insensitive to a uniform electric field, such as that caused by a uniform flow of water or the lateral translation of the sensor through the surrounding seawater. Rather, $\nabla^2\phi$ will exist only if the seawater has a relative rotary motion. It makes no difference whether the sensor or the water rotates.

The relationship between vorticity, velocity, potential gradients, and electric currents may be clarified by a few examples.

1) 2D CASE: VORTICITY AND MAGNETIC FIELD UNIFORM IN z

Consider a body of seawater in solid-body rotation about its vertical axis in a uniform vertical magnetic field. A cylindrical coordinate system (r, θ, z) is used with z vertical. Recall in solid-body rotation that vorticity is twice the angular rotation rate. For rotation about the $r = 0$ axis, the horizontal velocity in solid-body rotation is $\frac{1}{2}\omega_z r\mathbf{l}_\theta$, where θ is the angle in the cylindrical coordinate system [positive counterclockwise (CCW) from the x axis] and is a unit vector. The electric potential function from (3) is

$$\phi(r,\,\theta) = \int_0^r \left[\frac{1}{2}B_z\omega_z r - (J_r/\sigma)\right] dr. \tag{7}$$

The absence of vertical variations in the magnetic field or flow structure means that J_z and $\partial J_z/\partial z$ are zero. Continuity of electric current then requires that $\partial J_r/\partial r$ also be zero. Axial symmetry requires that $J_r = 0$ at $r = 0$. Hence, $\mathbf{J} = 0$ everywhere. Then,

$$\phi(r,\,\theta) = \frac{1}{4}B_z\omega_z r^2. \tag{8}$$

A set of three electrodes, equally spaced on a line in the horizontal plane and located at $r - l$, r, and $r + l$ would sense an average difference voltage of

$$\frac{\phi(r + l,\,\theta) + \phi(r - l,\,\theta) - 2\phi(r,\,\theta)}{2} = \frac{1}{8}B_z\omega_z[(r + l)^2 + (r - l)^2 - 2r^2)] = \frac{1}{4}B_z\omega_z l^2. \tag{9}$$

A two-axis unit would measure an *average* voltage of $\frac{1}{4}B_z\omega_z l^2$. A set of three electrodes equally spaced along the vertical axis would sense zero potential dif-

ference and contribute nothing to the sum obtained with two sets of electrodes oriented horizontally, say along the x and y axes. Hence, a sensor with two axes in the horizontal plane would observe an average voltage of $\frac{1}{4}B_z\omega_z l^2$. An average voltage is used so that the observed potential does not increase linearly with the number of sensor axes.

2) 3D CASE: UNIFORM VORTICITY IN DIPOLE MAGNETIC FIELD

Consider an infinite volume of seawater in solid-body rotation about the vertical (z) axis in a vertical dipole magnetic field. This is a realistic example that simulates what the EMVM (with its own dipole magnetic field) would observe in a patch of vorticity with a spatial scale that is large compared with that of the sensor. It also corresponds to the rotation of the EMVM in a comparatively large tank, such as was done in the laboratory to check the instrument's performance. More complex magnetic fields can be constructed by superposition from this elemental solution.

A derivation of the finite-difference equations can be based on Gauss's theorem for the case in which the vorticity and magnetic field are axially symmetric about the vertical axis, for example, solid-body rotation in a vertical dipole magnetic field. Integrating (5) over the volume V and applying Gauss's theorem yields

$$\int_A \nabla\phi \cdot \mathbf{n}\, dA = \int_V \mathbf{B} \cdot \boldsymbol{\omega}\, dV, \tag{10}$$

where $\mathbf{n}$ is the unit vector normal to the surface A. Consider a volume that is a right circular disk of radius R in the horizontal or x–y plane and thickness dz centered about $z = 0$. The left-hand integral in (10) can be expressed in terms of contributions from the surface at $r = R$ and from the top and bottom areas:

$$\int_A \nabla\phi \cdot \mathbf{n}\, dA = \int_{A_R} \partial\phi/\partial r\, dA + \int_{A_{\text{top}}} \partial\phi/\partial z\, dA + \int_{A_{\text{bot}}} \partial\phi/\partial z\, dA. \tag{11}$$

The contributions from the top and bottom surfaces cancel because of the assumed symmetry of the flow and of the magnetic field about the vertical axis. The potential and radial derivative at R can be expressed in terms of MacLaurin series, which can be manipulated to yield

$$\partial\phi(r)/\partial r = \frac{2}{r}[\phi(r) - \phi(0)] - \partial\phi/\partial r|_0 + \frac{r^2}{6}\partial^3\phi/\partial r^3|_0 + \text{higher-order terms}. \tag{12}$$

From the earlier analysis, we know that $\phi(r) = \frac{1}{4}\mathbf{B} \cdot \boldsymbol{\omega} r^2$. The term $\partial\phi/\partial r|_0$ is zero, and the third- and higher-order derivatives are zero (and will be small in general for vorticity patterns that are larger than the sensor). Thus we obtain

$$\int_{A_R} [\phi(R) - \phi(0)]\, dA = \frac{R}{2}\int_V \mathbf{B} \cdot \boldsymbol{\omega}\, dV \cdots. \tag{13}$$

Dropping the higher-order terms and expressing the integrals as averages gives

$$\langle \phi(R) - \phi(0) \rangle_{A_R} = \frac{\frac{1}{2}VR}{A_R}\langle \mathbf{B} \cdot \boldsymbol{\omega} \rangle_V, \tag{14}$$

where $\langle\ \rangle_{A_R}$ represents an average over the surface A_R and $\langle\ \rangle_V$ represents an average over the volume V.

The ratio of the volume ($V = \pi R^2 dz$) to the area ($A_R = 2\pi R dz$) of the disk-shaped body is $\frac{1}{2}R$; thus (14) becomes

$$\langle \phi(R) - \phi(0) \rangle_{A_R} = \frac{R^2}{4}\langle \mathbf{B} \cdot \boldsymbol{\omega} \rangle_V. \tag{15}$$

For a thin disk ($dz \ll R$), the ''volume'' average is more nearly an average over the surface between the origin and the radius R, and the ''surface'' area is more nearly an average around the circumference at the radius R. If electrodes are added from the x–y plane, the volume changes as does the bounding surface.

The simplest approximation of a spherical array is six electrodes at distances of $\pm R$ on the x, y, and z axes and one reference electrode at the origin. The corresponding area and volume are for the sphere of radius R about the origin. Recall that the vertical potential gradient is zero, and electrodes separated in that direction make no contribution to the average. Therefore, the average potential difference is two-thirds that of a single axis. The volume average of $\mathbf{B} \cdot \boldsymbol{\omega}$ times the ratio of volume to area is $\frac{1}{3}R^2\mathbf{B} \cdot \boldsymbol{\omega}$. Hence, for the 2D case where the volume integral is trivial,

$$\langle \phi(R) - \phi(0) \rangle_{A_R} = \frac{R^2}{4}\langle \mathbf{B} \cdot \boldsymbol{\omega} \rangle_V, \tag{16}$$

in confirmation of (15).

The utility of the vertical electrodes appears when flow is not two-dimensional and perpendicular to the axis of $\mathbf{B}$.

We interpret our measurements in terms of the integral expression because it explicitly accommodates spatially variables $\mathbf{B}$ and $\boldsymbol{\omega}$. In summary, the average potential from a set of equally distributed electrodes (minus the potential at the origin of the array) is interpreted as equal to the average scalar product of the magnetic field and vorticity. We use the robust relationship given in (15) for converting average electric potential differences into a component of the average vorticity parallel to the known applied magnetic field.

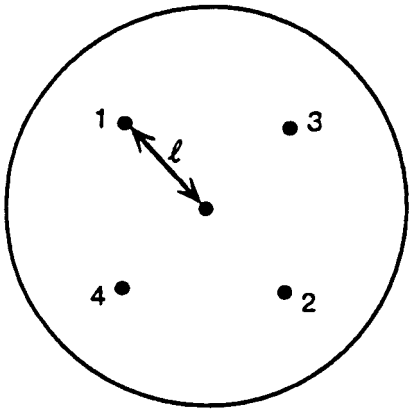

FIG. 1. EMVM electrode geometry (plan view). The sensor consists of five electrodes connected to the surrounding seawater by saltwater-filled tubes. The electrode tubes end about 6.25 cm off the face of the sensor. Under the face is a permanent magnet that provides a magnetic field of about 0.064 T at the ends of the electrode tubes. The magnetic field is positive out of the figure and is uniform to within ±3% within the radius *l*. The potential differences between the outer electrodes and the center electrode are denoted as e_i for $i = 1$–4.

c. Analytical solutions and numerical evaluations for a coil magnet

The previous section derived a general expression for interpreting potential measurements in terms of spatially averaged values of $\mathbf{B} \cdot \boldsymbol{\omega}$. No general expressions exist for interpreting potential gradients in terms of velocity. The interpretation depends on the spatial distribution of the magnetic field. Expressions for the magnetic field generated by a coil of wire of radius *a* are derived in appendix A.

d. Expressions for velocity and vorticity for a 2D sensor

A 2D EMVM sensor head consists of five electrodes connected by seawater-filled tubing to five locations within the applied magnetic field. The geometry of the measurement array is shown in Fig. 1. The voltages between the outer electrodes and the common center electrode are measured. Consider a right-hand coordinate system with *x*, *u*, and *U* in a horizontal direction positive to the left, *y*, *v*, and *V* positive CCW from the *x* axis, and *z*, *w*, and *W* positive up.

The four independent voltages can be combined to determine four flow variables. The four that are computed are two velocity components, one vorticity component, and a strain component averaged over the sensor scale. For a magnetic field that is positive in the *y* direction, the relations are (see appendix B)

$$\frac{\sqrt{2}}{4CBl}(e_1 - e_2 + e_3 - e_4) = \frac{U_1 + U_2 + U_3 + U_4}{4} \equiv u, \tag{17}$$

$$-\frac{\sqrt{2}}{4CBl}(e_1 - e_2 - e_3 + e_4) = \frac{W_1 + W_2 + W_3 + W_4}{4} \equiv w, \tag{18}$$

$$-\frac{e_1 + e_2 - e_3 - e_4}{CBl^2} = \frac{\partial w}{\partial z} - \frac{\partial u}{\partial x} = 2\frac{\partial w}{\partial z}, \tag{19}$$

$$\frac{e_1 + e_2 + e_3 + e_4}{Bl^2} = \frac{\partial u}{\partial z} - \frac{\partial w}{\partial x} = \omega_y, \tag{20}$$

where *l* is the magnitude of the distance vector $\mathbf{l}_i$ between the center and ends of individual electrode tubes, $e_i = \nabla\phi \cdot \mathbf{l}_i$, *B* is the magnitude of the magnetic field (assumed to be uniform over the sensor), and U_i and W_i are the spatially averaged velocity components across the *i*th electrode line. The head factor *C* is defined in (A5). From theory and experiment, we determined that the head factor is equal to about 0.5 for flow perpendicular to the applied magnetic field. The value will vary by 10%, depending on the spatial distribution of the magnetic field (see appendix B).

These relations assume that the same velocity components estimated at the intersection of orthogonal lines are equal. The following relations were used in (17) and (18):

$$(W_1 + W_2) - (W_3 + W_4) = 0 \tag{21}$$

and

$$(U_1 + U_2) - (U_3 + U_4) = 0. \tag{22}$$

In addition, the 2D form of the continuity equation was invoked in (19). There is a subtle point that should be made about the absence of the head factor in the expression for vorticity: There is no head factor for vorticity; vorticity does not induce any electric currents. The basis for this can be seen by summing the expressions for the individual electrode voltages in terms of velocity components and electric currents. The sum of the latter forms an expression of the form $\nabla \cdot \mathbf{J}/\sigma$, which is zero.

e. Response functions for velocity and vorticity for a 2D sensor

Because the electrodes are spatially separated, EMVM measurements of velocity and vorticity suffer from sensor attenuation. The effect is especially crucial for velocity gradients whose variances are mostly at small scales. Wyngaard (1969) described sensor responses of vorticity measurements obtained from a Kovasznay vorticity meter and other hot-wire arrays assuming isotropic homogeneous turbulence. The response function depends on the turbulence intensity (or

equivalently the Kolmogorov length scale) as well as on the sensor scale and configuration. Wallace and Foss (1995) reviewed measurements of vorticity in turbulent flows and concluded that the sensor separation from which the velocity gradient is estimated should not exceed about two to four Kolmogorov lengths.

To understand the EMVM measurements, it is necessary to determine the response functions. EMVM measurements were sampled while the vehicle was either profiled vertically or kept at fixed depths. The EMVM vehicle orients into the flow. It is convenient to express the measurements as streamwise (x, u, in the direction of the low-frequency flow), spanwise (y, v, in the horizontal direction perpendicular to streamwise), and vertical (z, w) coordinates. In either sampling mode, observed fluctuations are regarded as streamwise spatial variability of the flow field advected by the strong streamwise mean flow. The response function of the measured 1D streamwise spectrum is defined as

$$R_a(k_x, l) = \frac{\int dk_y \int dk_z \Phi_a(\mathbf{k}) R_a(\mathbf{k}, l)}{\int dk_y \int dk_z \Phi_a(\mathbf{k})}, \qquad (23)$$

where $a = u, w, \omega_y$, or $\partial_z w$, $\Phi_a(\mathbf{k})$ is the 3D wavenumber spectrum, $R_a(\mathbf{k}, l)$ is the 3D response function of the sensor, l is the sensor scale, and $R_a(\mathrm{k}_x, l)$ is the 1D response function. Explicit expressions of $R_a(\mathbf{k}, l)$ for the velocity components, vorticity, and strain rate are derived in appendix C. Note that $R_a(\mathbf{k}, l)$ is a property of the sensor configuration and, therefore, is independent of the actual wavenumber spectrum, $\Phi_a(\mathbf{k})$. Because the observed spectrum is a 1D projection of the 3D spectrum subjected to the 3D sensor response function, the 1D response function $R_a(\mathrm{k}_x, l)$ depends on the 3D wavenumber spectrum. To evaluate the 1D response function, the spectral form for homogeneous isotropic turbulence proposed by Pao (1965) is used (see appendix C). The 1D response functions for the streamwise and vertical velocities are independent of the turbulence intensity, whereas the response functions for vorticity and vertical strain are very sensitive to the turbulence intensity. This is because most of the variance of vorticity and strain is near the Kolmogorov length scale. The stronger the turbulence, the smaller the Kolmogorov length scale. However, the EMVM sensor measures vorticity fluctuations only at scales greater than the sensor scale l. Consequently, the ratio of the resolved rms vorticity and the true rms vorticity decreases monotonically with the increasing turbulence intensity. Details of the response function are described in appendix C.

3. Sensor and system design and construction

Several versions of the EMVM have been designed and constructed. From the use of these systems, we determined that it was important to

- control electrode offset and drift,
- provide stable and quiet voltage amplification,
- reduce flow distortion and vorticity generation by the sensor,
- eliminate ground loops and spurious electric currents,
- produce the maximum magnetic field, and
- design a robust system.

Some general comments about the electrodes and magnetic field are presented here, followed by a brief review of earlier systems and details of the present design.

a. Electrodes and salt bridges

The electrical connections between the seawater and the inputs to the amplifiers are through Ag–AgCl electrodes. The electrodes are a limiting factor in the performance of an EMVM system. In addition to producing a voltage offset (often over 1 mV), these electrodes possess temperature and salinity coefficients of about 350 μV K^{-1} and 530 μV psu^{-1}. Potting the electrodes in a conducting gel made from agar reduced the effects of both temperature and salinity changes. However, it was necessary to connect the chambers containing the electrodes to the locations of desired measurements with salt bridges, that is, tubes with insulating walls containing conducting agar gel or seawater. The salt bridges are terminated with small-diameter ceramic tubes (or straws). A 2D sensor consists of five electrodes, whereas a 3D array has seven.

b. Early electromagnet sensors

Early EMVMs used a synchronous demodulation scheme to separate the signal from the noise. In this method, the magnetic field was changed in a sinusoidal or square-wave modulation from positive to negative values at a frequency that was higher than the dominant electrode drift. The electrode voltages were then synchronously demodulated at the magnetic chopping rate.

A major problem with using a rapidly changing magnetic field is that it induces large voltages in the electrode circuits. A time-varying magnetic field acting on a residual loop area produces inductive coupling. Most of the residual loop area in a given sensor is in the electrical connections between the electrodes and the electronics. At the large magnetic field level needed to detect small levels of vorticity, such a level of induction noise is intolerable.

c. Present system

The complexity and power required of the electromagnet system were serious drawbacks in our effort to simplify the sensor and reduce its size, power requirements, and cost. A new sensor system was developed with the principal goals to

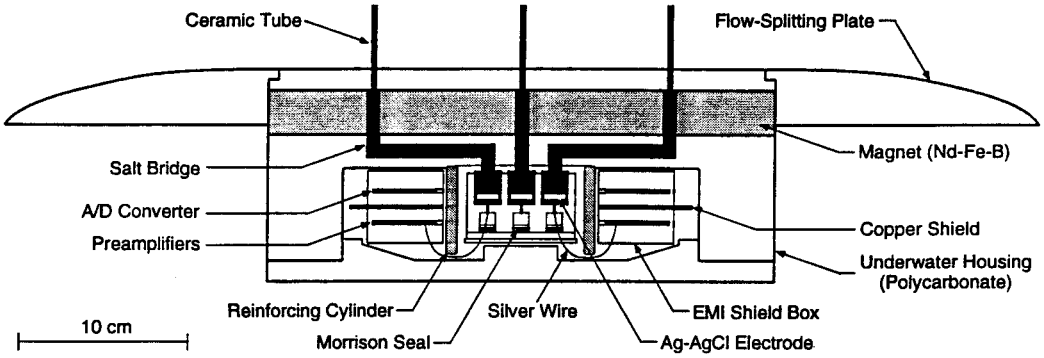

FIG. 2. EMVM sensor head (side view) with splitter plate. The view is a cross section along a diameter including electrode circuits for one axis. Details of some parts, such as O-rings and connectors, have been removed to simplify the diagram.

- eliminate the electric measurements along the axis of the magnetic field,
- produce less disturbance and be more symmetric to the flow,
- protect the electrodes for better noise performance,
- incorporate a permanent magnet into the sensor,
- isolate the sensor head with optical-fiber data links and batteries,
- construct the sensor out of plastic,
- separate the sensor from the main electronics, and
- keep flow away from the magnet except in the region of measurement.

The components of the present EMVM system are described below.

1) SENSOR HEAD

The present electromagnetic vorticity meter uses a permanent magnet with preamplifiers and analog-to-digital (A/D) converters in the sensor head. The EMVM sensor is built around the following components:

- electrodes: five Ag–AgCl electrodes, APL-UW manufacture;
- sensing tubes: five in a crossed array, Alumina ceramic, 2.5-mm OD, agar filled, extending 6.25 cm above the base plate;
- preamplifiers: AMP-01—differential, four channels, $\times 500$ gain, e_1, e_2, e_3, e_4;
- digitizers: analog devices AD7703, 20 bit, 20 Hz—four individual channels;
- magnet: NdFeB (37A) with a magnetic field of 0.064 T at 6.25 cm above the sensor;
- body: Lexan with a PVC flow-splitting plate to form a regular boundary layer;
- connectors: Impulse Enterprise, LPBH-3 (three-pin power), LPBH-9 (nine-pin digital).

The sensor head is shown in Fig. 2.

One important change was the decision to forego 3D measurements. The electrodes along the axis of the magnetic field were not providing an important signal. This was consistent with theoretical results derived earlier (see appendix A). It was decided to concentrate on an array of five electrodes in the x–y plane, normal to the principal axis of the magnet. The individual voltages between each outer electrode and the central reference electrode were used to compute velocity components normal to the magnet's axis and the vorticity aligned with the axis. One reason for this design was to eliminate asymmetry in the sensor. Earlier designs had structures that disturbed the flow in order to support electrode arms in the third direction.

The design achieves many of the goals but presents some difficulties. The ceramic tubes, or straws, are fragile and contribute a rather high impedance to the circuits. This high impedance results in significant Johnson noise and additional voltages resulting from the preamplifier bias current and/or current noise. However, the AMP-01 amplifiers have voltage and current noise characteristics that are favorable for this application. Since the impedance of the sensor source is about 5000 Ω, the amplifier needs this combination of properties to be effective. The velocity-induced signals are equal and opposite in sign at the input to amplifiers for electrode signals for e_1 and e_2, and these must cancel out for the vorticity calculation. This means that the gains of the preamplifiers must be the same. We want to observe vorticity-induced signals that are as small as 1×10^{-4} times the velocity-induced signals. To provide the required gain matching and stability, we have used precision Vishay resistors with a tolerance of 0.01% and a temperature coefficient of 2 ppm K^{-1}. A relatively low value of 500 was chosen for the overall preamplifier gain so that we could accommodate the large voltages (10 mV) produced by the combination of electrode offset potentials and velocity-induced signals.

The measurements are made above a smooth circular plate that has a tapered leading edge to reduce turbulence and is intended to slide through the relative flow with little angle of attack. A seawater-filled ceramic tube in a screw-in fitting electrically connects each electrode to the point of measurement in the seawater. Each ce-

ramic straw is connected to its electrode via an electrically conducting path provided by a solution of agar and seawater. The resulting gelatin-like substance is electrically conducting and avoids problems from air bubbles entrapped in tubes filled with just seawater. The encapsulation of the electrodes is intended to damp the temperature fluctuations and eliminate the salinity changes experienced by the electrodes. With a sensitivity of about 350 μV K^{-1} between similar electrodes at different temperatures, it is important to reduce this effect in the bandwidth of interest.

The electrode cups and straws are 8.9 cm apart on the plate and arranged in the form of a plus sign. The straws are 6.25 cm long and of the smallest diameter possible for the flow conditions. The splitter plate, electrode plenum, and magnet chamber are constructed of plastic to reduce electrical noise due to corrosion currents.

The electrodes, low-noise preamplifiers, 20-bit A/D converters, and optical-fiber drivers are installed in the sensor head, which is made of Lexan plastic and designed to withstand 300 db.

2) MAIN ELECTRONICS

The electronics provide timing signals and power to the sensor head, storage and transmission of data, and ancillary measurements, such as pitch, pitch rate, pressure, etc. In addition, the main electronics contain the electronics, batteries, data communication links, microprocessor, and connectors for recharging the batteries.

The main electronics can support two vorticity sensors, usually with both oriented in the spanwise direction, but sometimes with the second sensor oriented in the vertical direction. The pressure case is made from glass-filled Delrin.

The measurements are controlled, processed, and stored by an Onset Computer model TT-7 microcomputer with a 20-MB disk. The channels are stored at a 20-Hz rate on board, while 1-Hz averages are sent to the deck unit via an RS-422 link (see Fig. 3 for a block diagram).

The TT-7 samples all channels at 20 Hz except those for the altimeter and compass, which are sampled at their maximum rates of 2.5 and 2 Hz, respectively. The TPU subsection of the TT-7 accepts both the frequency inputs from the pressure, temperature, and electrical conductivity sensors and the serial I/O to and from the SonTek ADV current meter, KVH compass, and Datasonics altimeter. The raw data are compressed and stored on the internal 20-MB disk for later offloading. Once a second, in real time, averages and standard deviations of all the data channels are sent to the vorticity display and winch operator computers via the RS-422 on the tow cable.

The entire EMVM towed package is run from batteries to isolate it from the ship and so that it can be deployed autonomously. The isolation is important to prevent extraneous electric currents between the ship and the vehicle. These electric currents flowing in seawater could produce electric potentials in the water, which could contaminate the electrode measurements.

To provide as much electrical isolation as possible, several battery packs are used instead of DC-to-DC converters. In addition, no power is sent in the tow cable, and the RS-422 lines in the tow cable are optically coupled. Completely separate battery packs power the vorticity sensor preamplifiers and AD 7703 ADCs. This is to prevent electric currents from flowing between any part of the fish and the electrodes. The QSPI data connections to the vorticity sensor system are optically coupled to maintain that isolation. The serial connections to and from the SonTek current meter, compass, and altimeter are also optically coupled to prevent electric currents from contaminating the measurements.

4. Experimental deployments and scientific results

a. Instrumentation and operation

The latest version of the EMVM sensor, electronics, CTD unit, and altimeter is installed on an all-plastic tow body (Fig. 4) and has been deployed in several experiments in a tidal channel in Puget Sound. The tow body is designed to be a stable, flow-oriented platform for EMVM observations. The design provides for the mounting of two EMVMs, one on each side of the body, with both pointing horizontally or with one pointing vertically downward under the body. The tow body and sensor packages weigh about 307 kg (675 lb) in air and about 150 kg (330 lb) in seawater. The tow body alone weighs 216 kg (475 lb) in air. It is able to be towed at speeds up to 5 kt. The sensor suite and characteristics are presented in Table 1.

A Sea-Mac 3510 EAHL winch with 200 m of electromechanical tow cable was used to raise and lower the instrumented tow body. The Sea-Mac winch is an electrohydraulic unit with a 10-HP 230-Vac electric motor driving a variable-displacement hydraulic pump/motor combination. Haul-in and payout speed are continuously variable via a joystick control. The winch is outfitted with a slip-ring assembly from IEC Corp. (model IEL-BX-24) that has 24 contacts.

Blake Wire and Cable manufactured the 200 m of custom electromechanical cable, which has 24 conductors arranged as 12 twisted pairs covered by a polyethylene sheath. Exterior to the sheath is a Kevlar strength member rated at a working load of 450 kg. Finally, there is a polyurethane outer jacket. The overall diameter is 1.65 cm without a fairing. The cable was terminated at the underwater end with a 24-pin glass reinforced plastic underwater connector, type Seacon XSL-24-CCP, manufactured by Brantner & Associates. The tow cable was attached to the tow body with a Kevlar Chinese finger gripper.

The EMVM was deployed on several occasions in

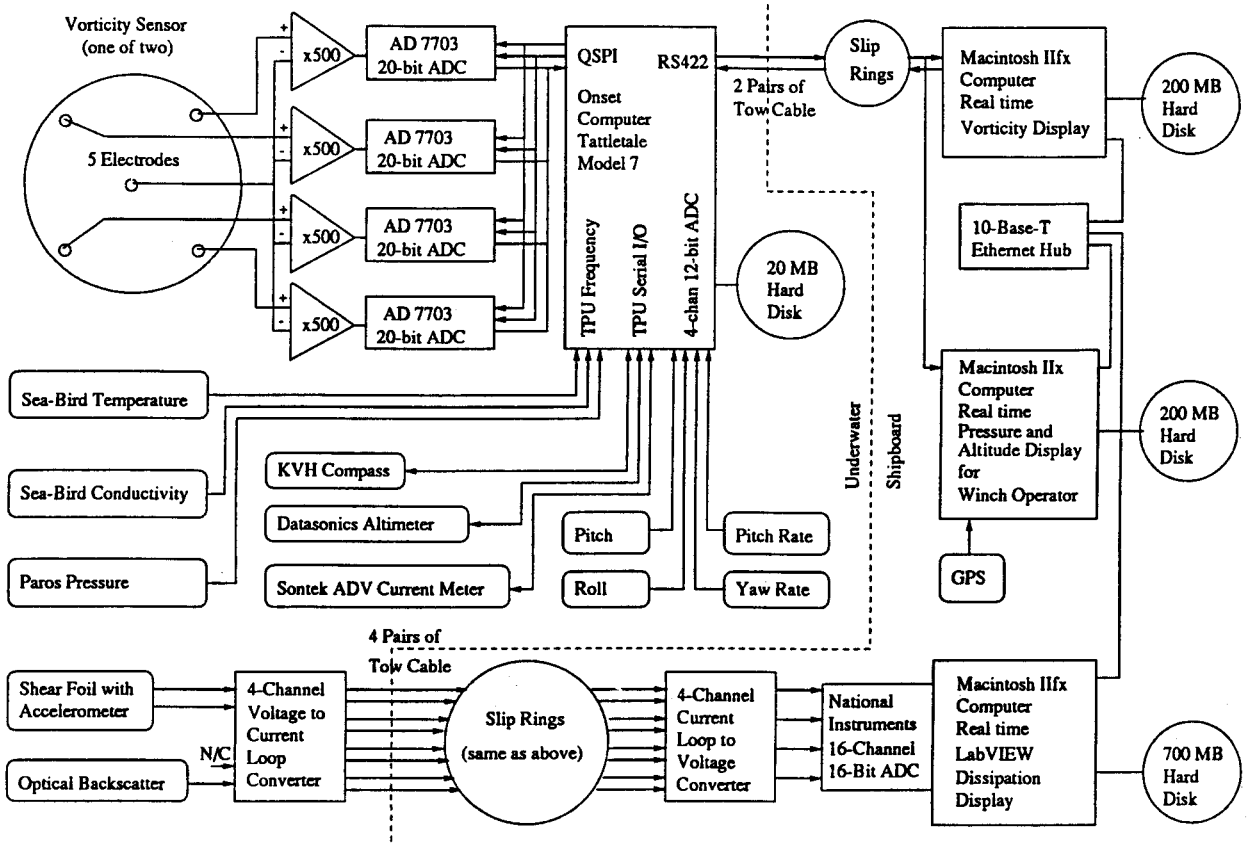

FIG. 3. Block diagram of electronics. Components and systems carried on the EMVM underwater vehicle are shown to the left of the dashed line. These devices are described in Table 1.

Pickering Passage, a narrow channel between Hartstene Island and the mainland. The channel often has a uniform bottom boundary layer (Sternberg 1968) and tidal currents of 1–2 kt. The channel has north–south and east–west reaches, permitting a choice of sites depending on wind and wave conditions. The observations reported here were taken from the R/V *Miller* while it was anchored at a site in the east–west reach near the entrance to Jarrell Cove on Hartstene Island.

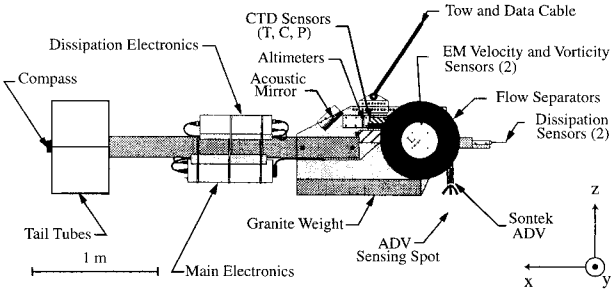

FIG. 4. Drawing of the EMVM tow body. The vehicle is made of PVC to avoid corrosion electric signals and carries about 200 kg of granite to provide stability. The instrumentation, detailed in Table 1, consists of the vorticity meter sensor and electronics, an acoustic Doppler velocimeter, an altimeter, temperature and conductivity sensors, a kinetic energy dissipation sensor, a turbidity sensor (or a second dissipation sensor), and attitude sensors (including a magnetic compass in the tail).

b. Data processing

Two EMVM sensors were used in the experiments. The sensors are denoted as *A* and *B*. Thus, the electrode

TABLE 1. Sensor suite: sources and specifications.

Measurement/ sensor	Manufacturer	Sample rate (Hz)	Resolution
Vorticity (two)	APL-UW	20	3×10^{-4} s^{-1}
Velocity (two)	APL-UW	20	10^{-5} m s^{-1}
Temperature	Sea-Bird	20	0.5×10^{-3} K
Conductivity	Sea-Bird	20	0.5×10^{-4} S m^{-1}
Pressure	Paroscientific	20	0.1 db
Altimeter	Datasonics	1	1 cm
Current meter	SonTek ADV	20	0.1 mm s^{-1}
Dissipation	APL-UW	400	10^{-8} W kg^{-1}
Turbidity	D&A Instruments	10	0.01 mg l^{-1}
Magnetic heading	KVH, Inc.	1	0.1°
Pitch	IC Sensors	20	0.035°
Roll	IC Sensors	20	0.035°
Pitch rate	Humphrey	20	$1 \times 10^{-3°}$ s^{-1}
Yaw rate	Humphrey	20	$1 \times 10^{-3°}$ s^{-1}

voltages expressed in (17)–(20) become e_iA and e_iB (i = 1–4). Computed variables carry the A or B designations, such as uA, wA, and vor$A$.

1) ELECTRODE OFFSETS

The electrode offsets are typically determined at the beginning and end of several hours of operation. The technique is to place a seawater-filled plastic bowl or shroud over the entire electrode array (i.e., the ceramic straws) and seal it against the PVC splitter plate. The shroud excludes velocity and vorticity (and stray electric currents) from the surrounding water. The instrument is raised and lowered in the water column to evaluate the effect of pressure on the electrode offset and to test for expected performance. It is important that the offsets do not have a pressure dependence; otherwise, the velocity and vorticity profiles would be contaminated.

The offsets were usually less than 1 mV. The electrode signals contain voltages of about 2 mV between points about 9 cm apart in a current of 0.5 m s^{-1} across the magnetic field of 0.064 T for a sensor with electrode axes oriented 45° to the flow. Electrode offset corrections are computed as a function of time based on a linear interpolation between the offsets determined at the start and end of observations. Tests in which offsets were determined in the middle of a 3-h-long experiment or when the shroud was left on for over 2 h showed a nonlinear deviation of 2.3 μV, which corresponds to a velocity of 0.4 mm s^{-1}.

2) VELOCITY

Once adjusted for the electrode offset, the electrode voltages are converted to velocity using the calibration of 174 m s^{-1} V^{-1}. The velocity axes, denoted velA_{12} and velA_{34}, are fixed to the sensor and rotate as the instrument pitches:

$$\text{vel}A_{12} = 174(e_1A - e_2A - e_{12}A_{\text{offset}}), \quad (24)$$

and

$$\text{vel}A_{34} = 174(e_3A - e_4A - e_{34}A_{\text{offset}}), \quad (25)$$

where $e_{12}A_{\text{offset}}$ and $e_{34}A_{\text{offset}}$ are the respective offsets. The observed velocity components are corrected for sensor orientation and compensated for sensor pitch.

Figure 5 compares the streamwise velocity component determined from the EMVM with that determined from the SonTek ADV. The 14% reduction in u_{EMVM} is consistent with the value of C for the normalized electrode separation distance of ~0.42 (see Fig. A4). The bias of −2.4 cm s^{-1} is consistent with the 0.5-m separation between the sensors in the mean vertical shear.

3) VORTICITY

The four electrode differences (μV) are combined to compute vorticity (s^{-1}) as follows:

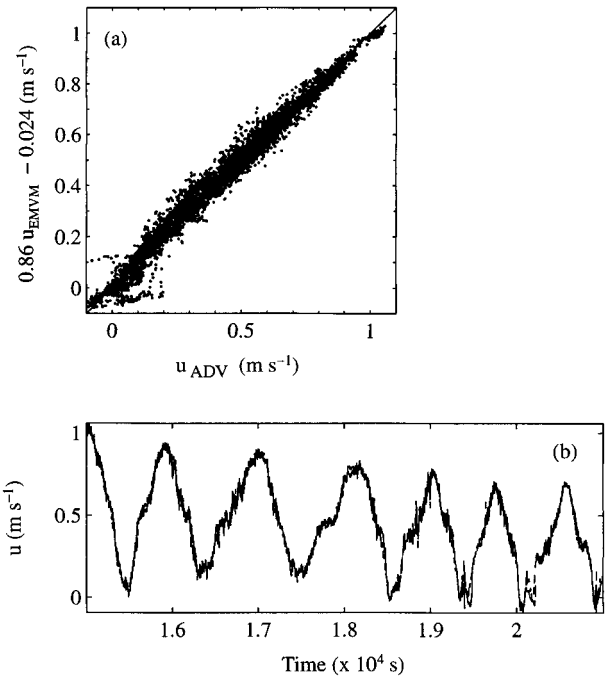

FIG. 5. Comparison of EMVM and ADV measurements of velocity while instruments were profiling up and down in the water column. The ADV sensor was located 0.5 m deeper than the EMVM. The correlation coefficient between the two velocities is 0.99. The best fit of the EMVM velocity is $u_{\text{ADV}} = 0.86u_{\text{EMVM}} - 0.024$ m s^{-1}. The scatterplot between the fitted EMVM velocity and the observed ADV velocity is shown in (a) and their time series are shown in (b).

$$\text{vor}A = -1.96 \times 10^{-3}(e_1A + e_2A + e_3A + e_4A - e_{1234}A_{\text{offset}}), \quad (26)$$

where $e_{1234}A_{\text{offset}}$ is the sum of the individual electrode offsets.

The effect of electrode offsets is greater for vorticity, which is a more sensitive measurement than velocity. The offset is not stable enough for the mean vorticity to be studied.

The EMVM cannot distinguish between vorticity in the water and rotation of the sensor about its sensitive axis. The adjustment of vor$A$ with the pitch rate measurements yields vorAa:

$$\text{vor}Aa = \text{vor}A + 2 \times \text{pitch rate}, \quad (27)$$

where the factor of 2 represents the relation between vorticity and solid-body rotation rate.

The seawater-filled shroud placed over the sensor to determine electrode offsets provides a means to verify (27) when the only vorticity measured is that produced by sensor rotation. The enclosed water does not respond when the sensor is rotated because there is not enough time and drag to produce significant rotation of the trapped water. Thus, apparent vorticity is observed when the sensor is shrouded and manually rotated, as when the cable is rapidly pulled or released. A comparison of vor$A$ and 2.0 × pitch rate is shown in Fig. 6 while the

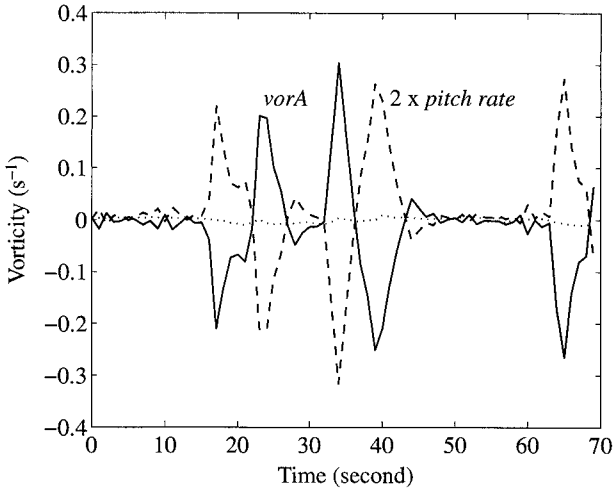

FIG. 6. Illustration of the compensation of vorticity for sensor rotation. This figure shows raw spanwise vorticity for sensor A (solid line), about twice the rate of change of sensor pitch (dashed line), and the sum of raw vorticity and 2 × pitch rate (dotted line). A multiplicative factor of 1.9, rather than 2.0, provides the largest correlation between vor*A* and pitch rate.

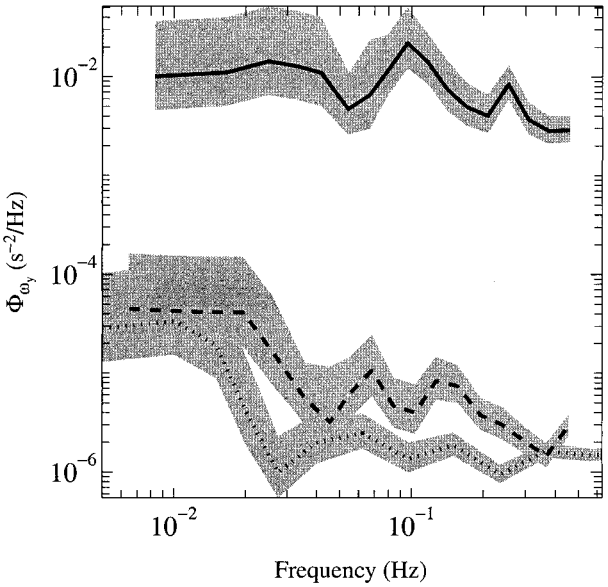

FIG. 7. Vorticity spectra for EMVM's sensor A at 20 mab during shrouded (dashed) and unshrouded (solid) observations. The shrouded data were taken about 15 min after the unshrouded. The dotted line is the spectra of observations taken in a still, saltwater-filled tank in the laboratory.

tow body was rotated (by grasping the tow cable between the winch and the block and pulling down rapidly). The best comparison is for a multiplicative factor of 1.9 rather than 2. The 5% reduction may reflect uncertainties in calibration for vorticity (e.g., electrode spacing, amplifier gain, magnetic field distribution), but it is thought to result from the momentum wakes of the electrode tubes. That is, when the instrument is rotated in stationary water, some water does move with the tubes, reducing the observed vorticity. This effect is consistent with the 5% reduction in sensitivity observed during the sensor shroud tests.

The EMVM has been operated in several modes: in a still seawater-filled tank, with the sensor under shrouds, and in normal (unshrouded) operation. Figure 7 shows the vorticity spectra resulting from operation in each of these modes. The shrouded and unshrouded observations were taken at 20 m above the bottom (mab) in Pickering Passage with the sensor in the spanwise orientation. The spectral noise level is about 10^{-6} s^{-2} Hz^{-1} out to a period of 50 s.

4) THEORETICAL AND OBSERVED SENSOR RESPONSES

The spectra observed during EMVM velocity and vorticity measurements are shown in Fig. 8, along with the predicted spectra based on the measured ε. Derivations of theoretical spectra and sensor response functions are described in appendix C. The EMVM measurements were taken within 0.5 m of the bottom in Pickering Passage during ebb tide while the instrument was sitting on the bottom. The water depth was about 25–30 m. The tidal current speed was about 1 m s^{-1} in the upper layer and about 0.5 m s^{-1} in the bottom boundary layer. The turbulence kinetic energy dissipation rate measured from shear probes was about 10^{-5} W kg^{-1}.

The observed streamwise velocity spectra show a clear spectral slope of $-5/3$ at low frequencies, a rolloff between 0.5 and 1 Hz, and a bump at 2–3 Hz. The theoretical spectra obtained using the measured ε agree remarkably well with the observations in both spectral level and spectral shape. The dip near 2 Hz in the observed spectra is not as sharp as the theoretical spectrum, presumably owing to varying mean flow speed and the assumed Taylor hypothesis.

The observed vertical velocity spectra also agree with the predicted spectra in general. At low frequencies, the observed spectra are weaker than the predicted spectrum. Since the sensors are 0.5 m from the bottom and the mean flow speed is about 0.5 m s^{-1}, variance of vertical velocity at frequencies smaller than 0.5 Hz is likely to be affected by the presence of the boundary.

The observed vorticity spectra are in good agreement with the theoretical vorticity spectrum of isotropic turbulence, including the effects of finite sensor size and sensor configuration. Note that the response function for the vorticity spectrum is very different from that for the velocity spectrum because most of the vorticity variance is at small scales, whereas most of velocity variance is at large scales.

The agreement between the observed and predicted spectra proves the quality and consistency of our measurements of ε, ω_y, u, and w. It also supports the response functions derived for the observed spectra.

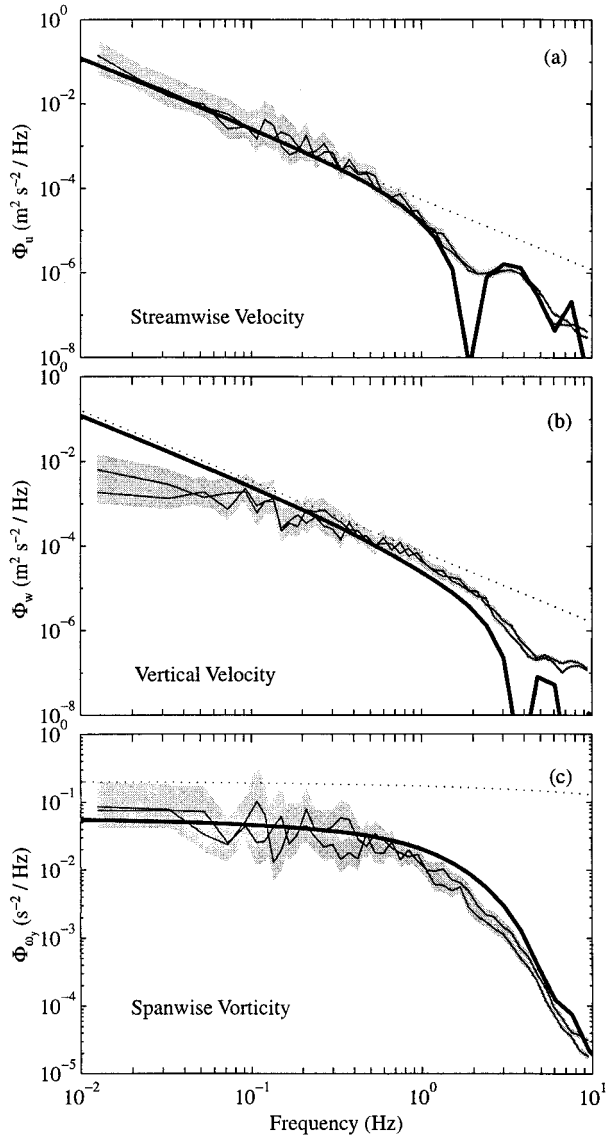

FIG. 8. Comparison of observed and predicted spectra. The thin curves and shading denote the spectrum observed for sensors A and B and their 95% confidence intervals. The thick solid and dotted lines represent the predicted spectra with and without the effects of the finite sensor scale, respectively. The predicted spectra are computed according to appendix C using the measured ε from the dissipation sensors on the EMVM vehicle.

c. Scientific applications and interpretations

The EMVM has been used extensively for profiling in Pickering Passage. The observations taken in homogeneous conditions over several days in October 1995 are discussed here with the view of evaluating the instrument's performance and comparing the results with laboratory and theoretical expectations.

1) MEAN STRATIFICATION

There was very little vertical stratification during the observations. The range of density variation was less than 0.01 kg m^{-3} ($\delta\rho/\rho = 10^{-5}$). The overall stratification was weak enough that homogeneous flow was assumed to be present.

2) MEAN VELOCITY PROFILES

In a homogeneous turbulent bottom boundary layer, the mean streamwise velocity profile, $U(z)$, can be described as

$$U(z) = \frac{u_*}{\kappa} \ln(z/z_o), \tag{28}$$

where u_* is the friction velocity and κ is von Kármán's constant (taken to be 0.4). Time-mean profiles are shown in Fig. 9a. The friction velocity is computed from the slope of $U(z)$ versus ln$z$, as plotted in Fig. 9b. It is 0.035 m s^{-1} with an uncertainty of about 20%. Bottom stress, τ, is related to u_* according to the relation

$$\tau = \rho u_*^2. \tag{29}$$

3) MEAN SPANWISE VORTICITY AND MEAN VERTICAL STREAMWISE SHEAR

The vertical structure of the mean spanwise vorticity can be computed and compared to the mean vertical shear of the streamwise velocity. The absolute value of vorticity cannot be determined because of the electrode offset voltages. The results are plotted in Fig. 10. The vertical structure of the means of the spanwise vorticity and streamwise shear are similar. This confirms that the other contribution to the mean spanwise vorticity, namely, the streamwise gradient of the mean vertical velocity component, is small.

4) TURBULENT VELOCITY AND VORTICITY

Profiles of the ratio of $\overline{w'^2}$ and $\overline{u'^2}$ rise from near zero to 0.6 at 2 mab and remain at less than 1 until a height of 15 m, where the ratio becomes abruptly greater than 1. The suppression of w as the bottom is approached could be expected, but the lack of equality of u and w higher is unexpected. Isotropy is expected at heights above the direct influence of the bottom.

Gross and Nowell (1983) reported that the ratio of perturbation and mean kinetic energies is about 2% within the bottom 1 m. We find that the ratio is less than 2%, but we do not get closer than 0.5 mab.

Figure 11 is a plot of enstrophy versus altitude. The enstrophy scales nearly as z^{-1} between 1.5 and 10 mab, where the log layer in mean velocity is strong and the Reynolds stress is about constant. The scaling of enstrophy is further discussed later.

5) TURBULENT MOMENTUM AND VORTICITY FLUXES

A classic quantity in wall turbulence is the Reynolds stress, defined as $-\overline{u'w'}$, where the bar is a time average.

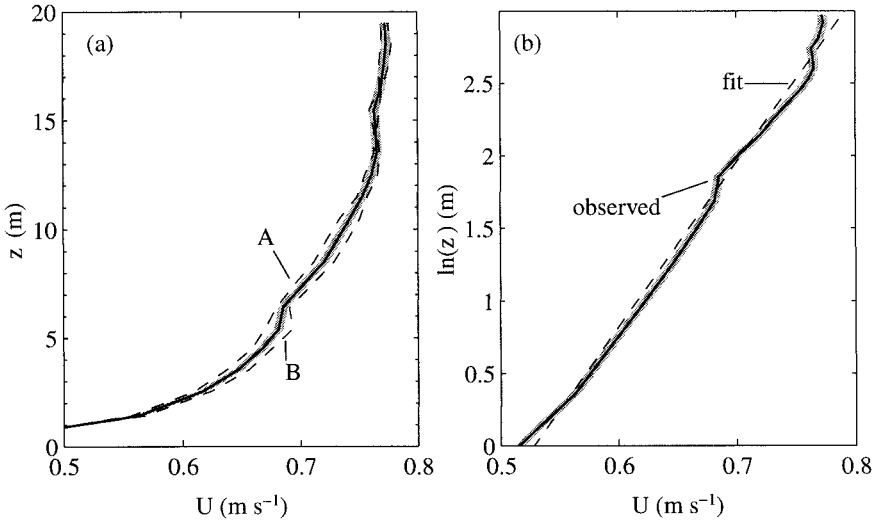

FIG. 9. Vertical profiles of time-mean streamwise velocity; z is the altitude measured from the bottom. (a) The two dashed lines are profiles obtained from sensors A and B, respectively. The solid curve is the average of the two mean profiles, and the shading marks its 95% confidence interval. (b) The observed streamwise mean velocity (solid curve) is fitted to log(z) (dashed curve) and shows an apparent logarithmic profile as found by previous studies.

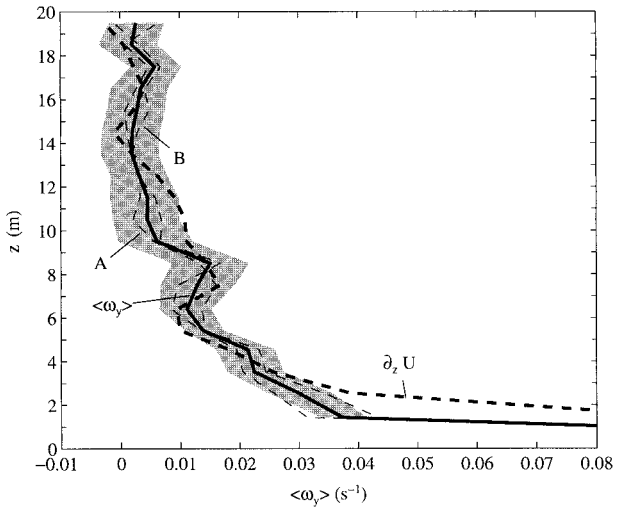

FIG. 10. Vertical profiles of mean spanwise vorticity and mean vertical shear. The two thin dashed curves are mean spanwise vorticity computed from sensors A and B and the thick solid curve represents their average. Because of the electrode drift, the time trend and mean of the spanwise vorticity are removed from the total record before calculating the vertical profile. Since the electrode drift is likely independent of the depth of the sensor, the vertical structure of the spanwise vorticity is unaffected by the demeaning and detrending processes, whereas the absolute value of the spanwise vorticity has been offset. To compensate for the offset, we set the mean spanwise vorticity equal to the mean vertical shear between 5 and 20 mab. The vertical structure of the spanwise vorticity is close to that of the vertical shear (thick dashed curve). The shading denotes the 95% confidence interval for the mean velocity shear.

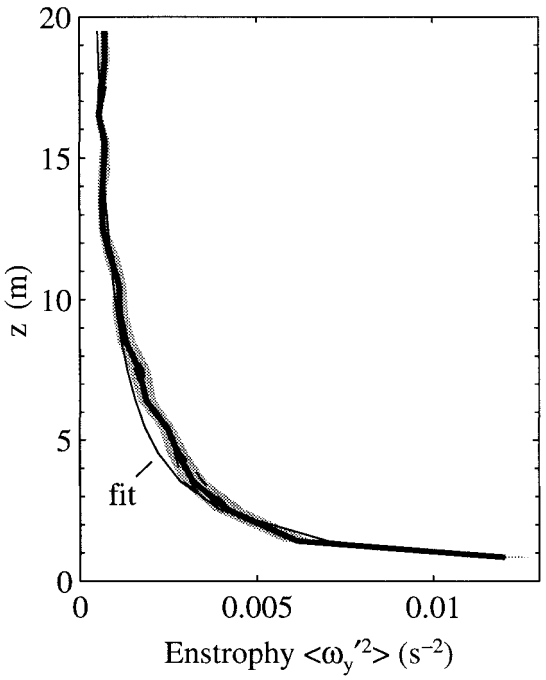

FIG. 11. Perturbation enstrophy profile. Dashed lines are for sensors A and B, which are nearly indistinguishable from the mean (thick line). Also shown as a thin line is the fit of the function z^{-1} to the observations over the depth interval 1–20 mab.

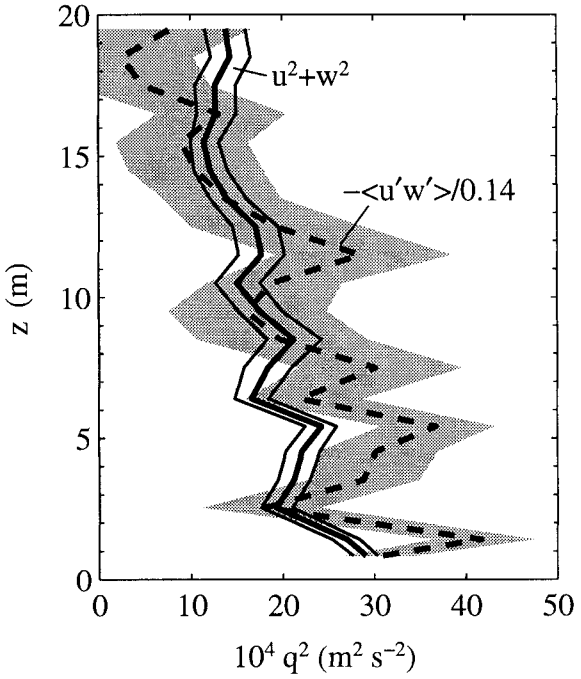

FIG. 12. Comparison of perturbation kinetic variance and Reynolds stress divided by 14%. The thick curve and the two thin solid curves are the mean vertical profiles of $u'^2 + w'^2$ and their 95% confidence interval. The dashed line and the shading are the scaled Reynolds stress and its 95% confidence interval.

Reynolds stress is a measure of the vertical flux of horizontal momentum. A negative value for $\overline{u'w'}$ indicates a flux of positive horizontal momentum downward to be absorbed in the bottom boundary layer through the mechanism of bottom friction. Gross and Nowell (1983) studied a tidal channel in Skagit Bay similar to that of Pickering Passage. They reported a value of $-\overline{u'w'}$, which was 14% of the perturbation kinetic energy $\overline{u'^2 + v'^2 + w'^2}$. The EMVM does not measure v', the spanwise perturbation velocity. It is assumed to be small compared with the streamwise and vertical components. Figure 12 shows the relationship between profiles of perturbation kinetic energy and the Reynolds stress normalized by 0.14^{-1}.

In a neutral, zero-pressure gradient, turbulent boundary layer, one would expect that $-\overline{u'w'} = u_*^2$. Gross and Nowell (1983) find that $-\overline{u'w'} = \frac{1}{2}u_*^2$. We find the factor is more like 0.4.

The vertical flux of horizontal momentum (i.e., Reynolds stress) profile is shown in Fig. 13a. The value of $-\overline{u'w'}$ projected to $z = 0$ is 5×10^{-4} m^2 s^{-2}. This compares to u_*^2 of 12×10^{-4} m^2 s^{-2}. One reason the friction velocity could be larger is because it is a combination of friction and form drag, whereas the Reynolds stress represents only the turbulent stress.

The vertical flux of spanwise vorticity profile, $\overline{w'\omega_y'}$, is shown in Fig. 13b. This flux is positive as expected for bottom-produced vorticity. Note that the perturbation vorticity is underestimated because of the finite size of the sensor (see appendix C).

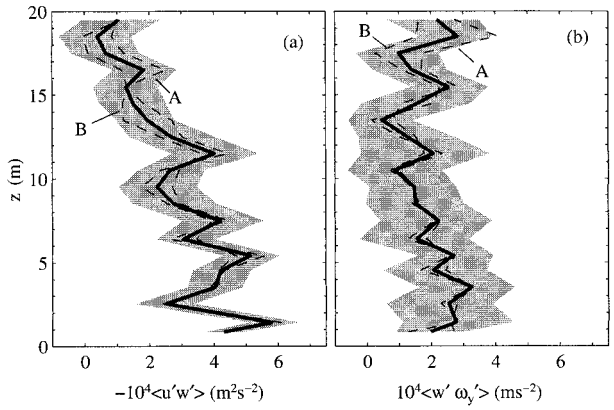

FIG. 13. Vertical profiles of (a) streamwise momentum flux and (b) spanwise vorticity flux. The two dashed curves are obtained from sensors A and B, and the thick solid curves are their averages. The shading represents the 95% confidence interval.

6) EDDY VISCOSITY

A formulation between the Reynolds stress and mean shear requires

$$-\overline{u'w'} = \nu_e \frac{\partial U}{\partial z}, \tag{30}$$

where ν_e is the eddy viscosity. The ratio of $-\overline{u'w'}$ and $\partial U/\partial z$, shown in Fig. 14, indicates eddy viscosities of $1\text{–}4 \times 10^{-2}$ m^2 s^{-1}. This determination of eddy viscosity is less than the often assumed value given by $\kappa u_* z$ and values reported in numerous coastal and tidal environments. The observations support a model consisting of a layer of constant stress in which the eddy viscosity increases nearly linearly with height (as the function $0.42\ z \times 10^{-3}$ m^2 s^{-1}) to a height of 10 mab or more. The thickness of the frictional sublayer (ν/u_*) is less than 1 mm. The turbulent boundary layer is much thicker, more than 1 m. A planetary boundary layer in a tidal channel is estimated by Bowden (1983) to be about $\pi(2\nu_e/\sigma)^{1/2}$, where σ is the tidal frequency (here the semidiurnal tide). This boundary layer is more than 50 m when fully developed.

In a similar fashion, the vertical vorticity flux and mean vertical gradient of vorticity can be related by

$$-\overline{w'\omega_y'} = \nu_e \frac{\partial \overline{\omega_y}}{\partial z}, \tag{31}$$

where ν_e is the eddy diffusivity of spanwise vorticity.

A comparison of the two estimates of eddy viscosity or diffusivity is shown in Fig. 14. The eddy diffusivity of spanwise vorticity flux is adequately resolved in our measurements at scales similar to those for the momentum and heat fluxes.

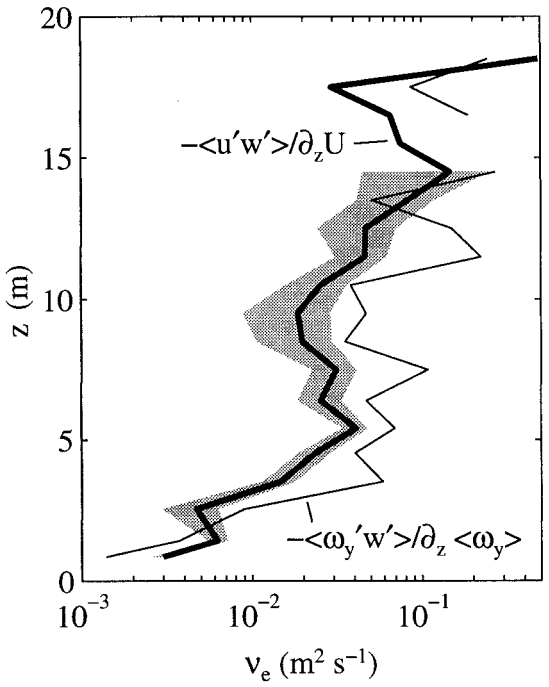

FIG. 14. Eddy diffusivity profiles based on momentum and vorticity fluxes. The thick line is the conventional determination of ν_e using the ratio of Reynolds stress and mean vertical shear. The shading is the 95% confidence interval. The thin line is ν_e computed from the ratio of the vertical vorticity flux of spanwise vorticity and mean spanwise vorticity. The computation is noisy, with large confidence intervals (not shown). A common parameterization of the vertical eddy viscosity, $\kappa u_* z$, is also plotted for $u_* = 0.035$ m s^{-1}.

5. Summary and conclusions

An electromagnetic velocity and vorticity meter, EMVM, has been developed to measure small-scale velocity and vorticity in seawater. It is based on the principles of motional induction and senses quantities on scales larger than its 20-cm electrode array. A permanent magnet provides the magnetic field, and electrodes are connected to the voltage measurement points by conducting salt bridges. The response function of the EM sensor has been determined, and profiles of velocity, vorticity, dissipation, and water properties have been collected in a turbulent tidal channel. Laboratory and field evaluations support rms noise levels of about 10^{-4} m s^{-1} for velocity and 10^{-3} s^{-1} for vorticity. The field evaluations have demonstrated satisfactory performance of the EMVM system and confirmed some classic boundary layer results. There was much concern that the fragile ceramic tubes used for the electrode lines would break during extensive operations. In fact, none of the ceramic tubes broke during the measurements, which were taken over a period of four maximum ebb flows.

For the current configuration, variations in electrode offsets were not important for periods less than 100 s. Earlier versions had tried to reduce the effect of electrode drift by using an electromagnet powered by a current modulated by a square wave. The benefit of the modulation and subsequent synchronous demodulation was more than offset by the liabilities of a lower magnetic field and the extra complexity. Experiments with a permanent magnet showed that electrode drift did prevent the determination of absolute vorticity but was insignificant for determining velocity. The vorticity record was detrended by removing mean and linear components. Because the data were collected during many vertical profiles, the detrending process did not suppress the vertical variation of vorticity. Perturbation quantities were not affected by the electrode offset.

The mean velocity and mean vorticity measured in the field in a tidal channel are consistent with a classic turbulent log layer, and the eddy contributions also exhibit ''law of the wall'' characteristics comparable to the results found by previous investigators. In particular, we find that $-\overline{u'w'}/q^2$ is 15%, comparable to the 14% reported by Gross and Nowell (1983) in a similar tidal channel. The ratio of Reynolds stress to mean vertical shear was about 1–4 $\times$ 10^{-2} m^2 s^{-1} in the lower 10 m. This estimation of an eddy viscosity is comparable to eddy viscosities computed from the vorticity flux. This was not anticipated because the EMVM does not resolve small-scale fluctuations of vorticity. The explanation is that the EMVM adequately resolves the covariance between vertical velocity and spanwise vorticity in a turbulent bottom boundary layer.

The vorticity observations obtained in this experiment are unique. The perturbation enstrophy profile scales as z^{-1}. This scaling is reasonable for measurements in a constant stress layer in which $\varepsilon = u_*^3/\kappa z$, provided that $C \times \omega_y^2 = \varepsilon$, where C is a constant.

The velocity measurements confirm expectations from previous measurements and modeling of tidal channels. The vorticity and enstrophy observations behave in reasonable ways. That is, the mean spanwise vorticity agrees with the mean streamwise vertical shear, and the perturbation enstrophy exhibits a monotonic increase toward the bottom and a scaling consistent with a constant stress layer. Future work will concentrate on validating ε values derived from the vorticity observations. Also, more recent observations include one sensor oriented in the vertical direction. These new data will be included in future studies.

Acknowledgments. This research was supported by the Office of Naval Research under Grant N00014-95-1-0222. The project was initiated with support from Ken Ferer addressing requirements of the Oceanographer of the Navy. The authors thank Mike Welch and Victor Lo for their efforts in the design and fabrication of the latest EMVM and Gordon Welsh and Robert Leathers for their expert assistance in the development of the tow body and its use in the field. Gordon Welsh designed the EMVM vehicle and sensor mounts. Michael Gregg provided guidance and software for computing kinetic en-

ergy dissipation rates from shear foil data. Eric Kunze has provided numerous suggestions and encouragement.

APPENDIX A

Analytic and Numerical Computations of Potential Field in EMVM

Consider an infinite volume of seawater in solid-body rotation about the vertical (z) axis in a magnet field that is symmetrical about the vertical axis. This is a realistic example that simulates what an EMVM (with its own dipole magnetic field) would observe in a patch of vorticity with a spatial scale that is large compared with that of the sensor. It also corresponds to the rotation of an EMVM with its own dipole magnetic field in a comparatively large tank, as was done in the laboratory to check the instrument's performance. More complex magnetic fields can be constructed by superposition from this elemental solution.

The symmetry of the problem places constraints on the electric current paths. For example, the electric currents must be antisymmetric about the $z = 0$ plane (i.e., mirror images). This statement is proved as follows. Consider the line in the z direction that passes through the origin. For a volume in solid-body rotation about this line, the vertical electric currents must change sign at the origin. That is, the currents are an odd function with respect to z. This fact can be seen by considering the induction terms along the z axis. The induction term, $\mathbf{v} \times \mathbf{B} \cdot \mathbf{l}_z$, from (3) is zero on the z axis. Hence,

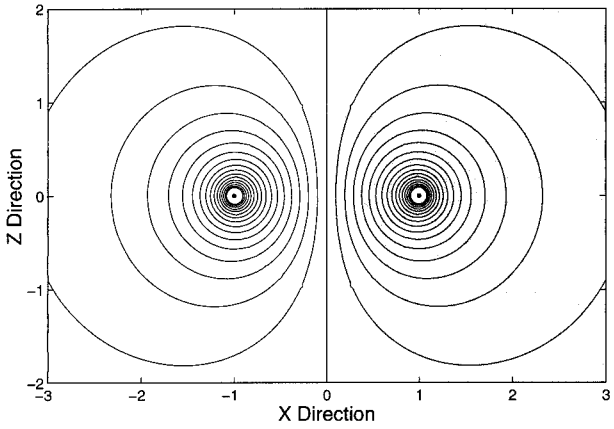

FIG. A1. The potential field ϕ generated by uniform flow in the presence of a magnetic field generated by an electric current (I) passing through a thin circular loop of radius a. Distances are normalized by a. Gray shading denotes negative values. The view is with the water flow coming out of the page. The contour increment is 0.05 and is nondimensional. To rescale the values, multiply by UaB_0, where U is the water speed, a is the radius of the loop, and B_0 is the vertical magnetic field in the center of the loop (which is $\mu_0 I/2a$).

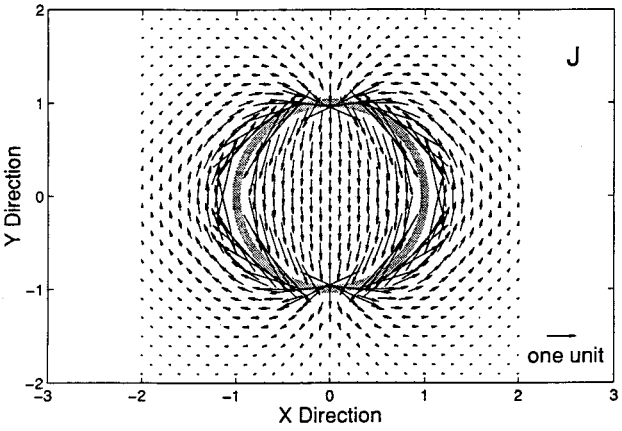

FIG. A2. Vector plots of the electric current density **J** produced by a uniform flow in the magnetic field of the current loop. The view is of the x–y plane, looking down from above. Distances are normalized by the radius of the coil producing **B**. The uniform flow is from left to right (positive x direction). Within the coil, **J** is in the same direction as $\mathbf{v} \times \mathbf{B}$. Since $\nabla\phi = \mathbf{v} \times \mathbf{B} - \mathbf{J}/\sigma$, the value of $\nabla\phi$ is less than expected from $\mathbf{v} \times \mathbf{B}$ alone. The vectors are nondimensionalized, scaled by $\sigma U\mathbf{B}_0$, where $\mathbf{B}_0$ is the magnetic field strength in the center of the field coil (i.e., $\mu_0 I/2a$).

$$\phi(0) - \phi(-\infty) = -\int_{-\infty}^{0} J_z \, dz \tag{A1}$$

and

$$\phi(0) - \phi(\infty) = \int_{0}^{\infty} J_z \, dz. \tag{A2}$$

Because the magnetic field is of finite extent, it is necessary that the potential be a constant at infinity; that is, $\phi(\infty)$ must be the same value as $\phi(-\infty)$. It is convenient to take this value to be zero. The only form for J_z that will satisfy the above expression is for it to be an odd function of z. In this way, the potential at the origin is the same regardless of whether the integration toward the origin is along the positive or the negative z axis. Another consequence is that the electric currents converging on the origin along the z axis are compensated by electric currents flowing outward on the x–y plane. Thus the horizontal current along the x axis must also be an odd function of x and of the opposite sign as that for z. That is, if J_z is positive for $z > 0$, then J_x must be negative for $x > 0$. The induction term, $\mathbf{v} \times \mathbf{B} \cdot \mathbf{1}_x$, integrates to zero along the line from infinity to the origin. Hence it makes no contribution to the potential at the origin.

The consequence is that integrating from infinity along the z axis yields a potential at the origin that is of opposite sign to that obtained by integration along the x axis. The potential at the origin must be independent of the path of integration. The only way for the potential to be independent of the path of integration is for J_x to be zero on the x axis, for J_y to be zero on the y axis, and for J_z, to be zero on the z axis. This argument

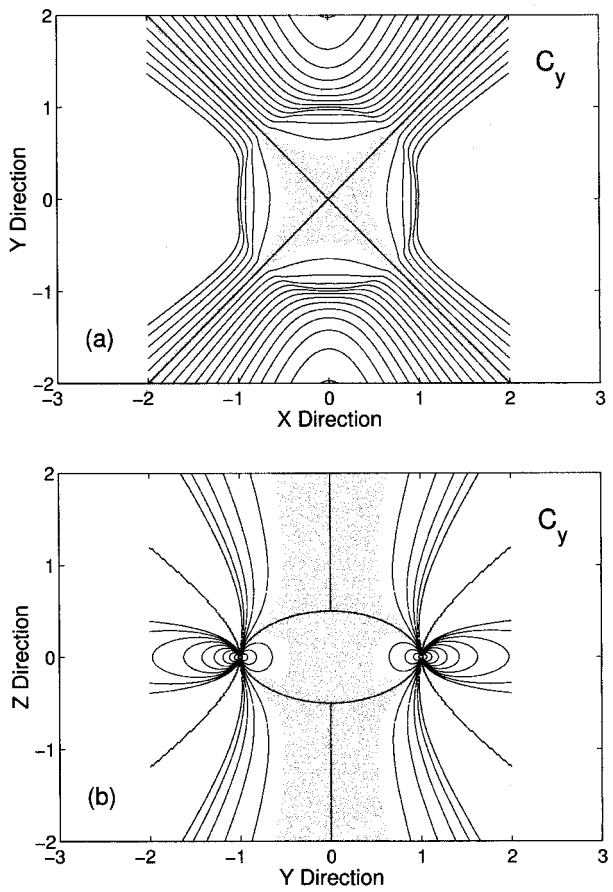

FIG. A3. Contours of the nondimensional correction factor **C** for flow from left to right in the magnetic field generated by the current loop. The contour increment is 0.1. The light gray shading denotes negative values (whose contours are not shown), while the dark gray indicates the region where **C** is between 0.45 and 0.55. (a) Contours in the *x–y* plane. (b) Contours in the *y–z* plane. Note that for most of the region within the coil, the correction factor is between 0.45 and 0.55.

does not exclude electric currents flowing in other parts of the space, but a formal solution given later demonstrates that $\mathbf{J} = 0$ everywhere. Hence, there can be no electric currents flowing as a consequence of solid-body rotation in a dipole magnetic field.

The previous discussion derived relationships between potential measurements and vorticity using a minimum of mathematical complexity. Now analytical solutions are derived for uniform flow and uniform solid-body rotation. In this analysis, we will assume that the magnetic field is generated by a thin coil. For the assumptions made earlier for (3) and (4), the governing equations are

$$\nabla\phi = \mathbf{v} \times \mathbf{B} - \mathbf{J}/\sigma \quad \text{and} \quad \nabla^2\phi = \mathbf{B} \cdot \nabla \times \mathbf{v}. \tag{A3}$$

The goal is to develop analytical expressions for ϕ and **J** based on specified forms of **B** and **v**. The analysis is presented by Sanford et al. (1995) and will not be repeated here. The analysis was conducted for flow in the

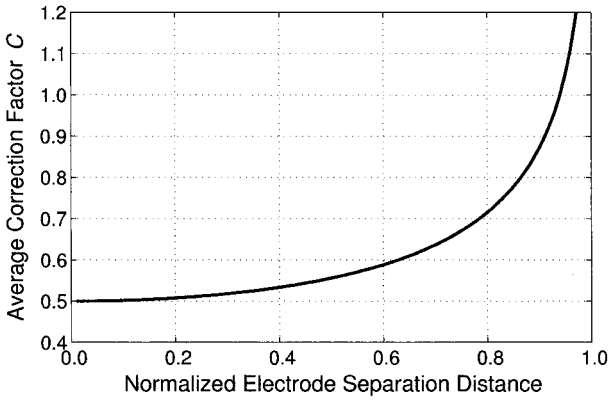

FIG. A4. The correction factor **C** as a function of electrode separation computed for uniform flow past a four-electrode array. The separation distance has been normalized by the radius of the magnetic field coil.

presence of the magnetic field generated by a simple wire loop. The electrical responses for spatially uniform rectilinear and rotary flows were determined analytically and evaluated numerically. Only the graphical results of the analysis will be presented here.

The magnetic field produced by an electric current (I) in a thin coil of radius a can be expressed in a spherical coordinate system (r, θ, γ), where the variables are radius, azimuth in the x–y plane (CCW from x axis), and altitude (CCW from the x–y plane).

If one assumes a flow of uniform horizontal velocity (U) with no vertical component or variation, then

$$\mathbf{v} = U\hat{\mathbf{i}} = U\sin\theta\cos\gamma\hat{\mathbf{r}} + U\cos\theta\cos\gamma\hat{\boldsymbol{\theta}} + U\sin\gamma\hat{\boldsymbol{\gamma}}. \tag{A4}$$

For uniform flow, the velocity field is irrotational ($\nabla \times \mathbf{v} = 0$), so the problem reduces to solving for the Laplacian of the potential, $\nabla^2\phi = 0$. The ϕ field is shown in Fig. A1. For uniform flow, the potential field has no curvature in the center, and thus no vorticity would be measured. This is expected for uniform flow. To infer velocity from $\nabla\phi$, however, the current density must be known. The induction equation, (3), is rewritten as

$$\begin{aligned}\nabla\phi &= \mathbf{C} \cdot \mathbf{v} \times \mathbf{B} \\ &= \hat{\mathbf{i}}[\mathbf{C}_x \cdot (\mathbf{v} \times \mathbf{B})] + \hat{\mathbf{j}}[\mathbf{C}_y \cdot (\mathbf{v} \times \mathbf{B})] \\ &\quad + \hat{\mathbf{k}}[\mathbf{C}_z \cdot (\mathbf{v} \times \mathbf{B})],\end{aligned} \tag{A5}$$

where **C** is a diagonal tensor representing a correction, or "head" factor, and $\hat{\mathbf{i}}$, $\hat{\mathbf{j}}$, and $\hat{\mathbf{k}}$ are unit vectors in the x, y, z directions, respectively. The head factor will be different for each axis and depends in general on the forms of the magnetic field, fluid flow, and configuration of the electrode array. The magnitude of the head factor in the ith direction is $C_i = 1 - (\mathbf{J} \cdot \hat{\mathbf{i}}/\sigma)/(\mathbf{v} \times \mathbf{B}) \cdot \hat{\mathbf{i}}$.

A visualization of the circulation of **J** fields is presented in Fig. A2. Note that the vectors are about one-half a scaled unit. Hence $C_y \sim 0.5$. Other views of the structure of C_y for a flow in the positive x direction are

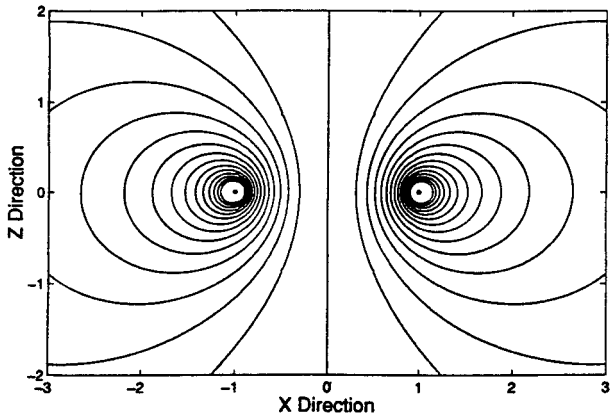

FIG. A5. The potential field ϕ generated by solid-body rotating flow around the z axis in the presence of the magnetic field generated by a current loop. The view is with the flow coming out of the page on the left side and back in on the right side. Unlike for uniform flow, ϕ here is positive everywhere. The contour increment is 0.05 and is nondimensional. To rescale the values, multiply by $(\omega/2)a^2B_0$, where ω is the relative vertical vorticity, a is the radius of the loop, and B_0 is the vertical magnetic field in the center of the loop (i.e., $\mu_0 I/2a$).

plotted in Fig. A3. Near the center of the coil, the C_y values are nearly uniform at 0.5. Thus the velocity estimated from $\nabla\phi$ measurements alone is only half what exists. While Fig. A3 shows pointwise calculations of C_y, Fig. A4 presents the effective C_y as a function of the normalized separation distance between the center and perimeter electrodes.

Now consider a flow in solid-body rotation about the z axis. For a spherical coordinate system, the vorticity, ω, of the system is

$$\omega\hat{\mathbf{z}} = \omega\cos\theta\hat{\mathbf{r}} - \omega\sin\theta\hat{\boldsymbol{\theta}}. \tag{A6}$$

The potential field, ϕ, for the velocity field in solid-body rotation is shown in Fig. A5. All potential contours are positive and correspond to the integral of $\mathbf{v} \times \mathbf{B}$ from the axis of the coil. That is, there are no circulating electric currents (i.e., $\mathbf{J} = 0$). This is as was indicated in the more heuristic analysis in this appendix.

APPENDIX B

Electric Field and Velocity Components for the 2D Sensor

A 2D EMVM sensor head consists of five electrodes in five locations above a permanent magnet. The geometry is shown in Fig. 1. The voltages induced by flow between the center electrode and each outer electrode are measured. These four independent voltages allow the determination of an equal number of flow characteristics, for example, two components of velocity and two gradient terms. According to (3), the potential gradient induced in the seawater by a flow $\mathbf{v}$ through a magnetic field $\mathbf{B}$ is

$$\nabla\phi = \mathbf{v} \times \mathbf{B} - \mathbf{J}/\sigma, \tag{B1}$$

where ϕ is the electric potential, $\mathbf{J}$ is the electric current density, and σ is the electrical conductivity of the seawater.

Consider the x–z plane of a right-hand coordinate system with x and u positive to the left, y and v positive out of the plane (i.e., 90° CCW from the x axis), and z and w positive up. For a sensor as depicted in Fig. 1 with a uniform magnetic field B (positive in direction out of the sensor, i.e., out of the x–z plane) and spatially averaged velocity components of U and W, the potentials $(e_1, \ldots, e_4)$ at the ends of the electrode lines minus the potential of the center electrode are

$$\frac{\sqrt{2}}{l}e_l = BU_l - BW_1 - \frac{J_{x1}}{\sigma} - \frac{J_{z1}}{\sigma} \tag{B2a}$$

$$\frac{\sqrt{2}}{l}e_2 = -BU_2 + BW_2 + \frac{J_{x2}}{\sigma} + \frac{J_{z2}}{\sigma} \tag{B2b}$$

$$\frac{\sqrt{2}}{l}e_3 = BU_3 + BW_3 + \frac{J_{x3}}{\sigma} - \frac{J_{z3}}{\sigma} \tag{B2c}$$

$$\frac{\sqrt{2}}{l}e_4 = -BU_4 - BW_4 - \frac{J_{x4}}{\sigma} + \frac{J_{z4}}{\sigma}, \tag{B2d}$$

where l is the magnitude of the distance vector $\mathbf{l}_i$ between the center and the ends of the individual electrode tubes, $e_i = \nabla\phi \cdot \mathbf{l}_i$, B is the magnitude of the magnetic field (assumed to be uniform over the sensor), U_i and W_i are the spatially averaged velocity components across the ith electrode line, and J_{xi} and J_{zi} are the electric current density components along each electrode line.

A difficulty is that no independent measurement of $\mathbf{J}/\sigma$ is obtained. That is, measuring $\nabla\phi$ along a given vector line ($\mathbf{l}$) and knowing $\mathbf{B}$ is not enough uniquely to determine $\mathbf{U}$ (Shercliff 1962). What is determined by the potential measurements is the difference between the source term $\mathbf{U} \times \mathbf{B}$ and the response term $\mathbf{J}/\sigma$. Because the induction is a linear problem, the response is proportional to the source. If the magnetic field and flow are known, this response function can be computed. Usually, it is determined empirically from calibrations in a tow tank or in the field. Both methods have been applied in this work. The interpretation equation used is

$$\nabla\phi \cdot \mathbf{l} = \Delta\phi = C\mathbf{U} \times \mathbf{B} \cdot \mathbf{l}. \tag{B3}$$

The factor C is defined in (A5) and is for the axis $\mathbf{l}$. We determined that the head factor, C, is equal to about 0.5 for flow perpendicular to the applied magnetic field. The value will vary by 10% depending on the spatial distribution of the magnetic field.

Now, if we write (B3) along the z axis,

$$BU - \frac{J_z}{\sigma} = CBU. \tag{B4}$$

Similarly, for the x axis,

$$BW - \frac{J_x}{\sigma} = CBW. \tag{B5}$$

Hence, the combinations of e_1 and e_3 yield

$$\frac{\sqrt{2}}{CBl}(e_3 - e_1) = (W_3 + W_1) + (U_3 - U_1) \tag{B6}$$

and

$$\frac{\sqrt{2}}{CBl}(e_3 + e_1) = (U_3 + U_1) + (W_3 - W_1). \tag{B7}$$

The combinations of e_2 and e_4 yield

$$\frac{\sqrt{2}}{CBl}(e_2 - e_4) = (W_2 + W_4) - (U_2 - U_4) \tag{B8}$$

and

$$\frac{\sqrt{2}}{CBl}(e_2 + e_4) = -(U_2 + U_4) + (W_2 - W_4). \tag{B9}$$

These expressions are combined to form (17)–(20).

APPENDIX C

EMVM Sensor Response

If (17)–(20) are transformed into Fourier space, EMVM velocity, vorticity, and strain rate can be represented as

$$u = \int d\mathbf{k}\tilde{\phi}(\mathbf{k}) \exp[i\mathbf{k}\cdot\mathbf{x}_0] \times \left\{\frac{i\cos(lk_x/\sqrt{2})\sin(lk_z/\sqrt{2})}{CBl/\sqrt{2}}\right\}, \tag{C1}$$

$$w = \int d\mathbf{k}\tilde{\phi}(\mathbf{k}) \exp[i\mathbf{k}\cdot\mathbf{x}_0] \times \left\{\frac{i\cos(lk_z/\sqrt{2})\sin(lk_x/\sqrt{2})}{CBl/\sqrt{2}}\right\}, \tag{C2}$$

$$\omega_y = \int d\mathbf{k}\tilde{\phi}(\mathbf{k}) \exp[i\mathbf{k}\cdot\mathbf{x}_0] \times \left\{\frac{4[\cos(lk_x/\sqrt{2})\cos(lk_z/\sqrt{2}) - 1]}{Bl^2}\right\}, \tag{C3}$$

and

$$\partial_z w = \int d\mathbf{k}\tilde{\phi}(\mathbf{k}) \exp[i\mathbf{k}\cdot\mathbf{x}_0] \times \left\{\frac{-\sin(lk_x/\sqrt{2})\sin(lk_z/\sqrt{2})}{CBl^2/2}\right\}, \tag{C4}$$

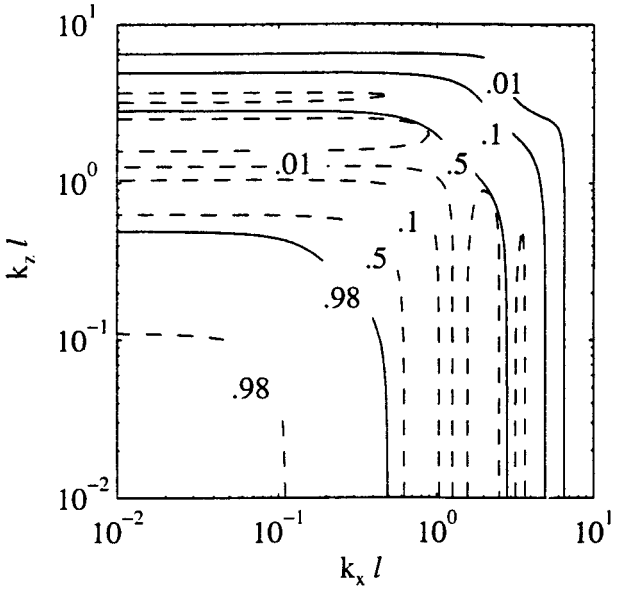

FIG. C1. Contours of EMVM response functions for vorticity (solid lines) and strain (dashed lines) in 2D wavenumber domain. The wavenumbers k_1 and k_2 represent wavenumbers in the two orthogonal directions and l is the length of the electrode separations. If the sensor is oriented vertically, then the wavenumbers are k_x and k_y. Similarly, if the sensor is oriented in the spanwise direction, the wavenumbers are k_x and k_z.

where $\tilde{\phi}$ is the Fourier coefficient of ϕ, l is the separation of electrodes from the center $\mathbf{x}_0$, $\mathbf{k}$ is the 3D wavenumber vector, and k_x and k_z are the streamwise and vertical wavenumber components. For a perfect sensor with infinitesimal electrode separations, measurements of velocity, vorticity, and strain at the center of the sensor would be

$$u = \int d\mathbf{k}\tilde{\phi}(\mathbf{k}) \exp[i\mathbf{k}\cdot\mathbf{x}_0]\left\{\frac{ik_z}{CB}\right\}, \tag{C5}$$

$$w = \int d\mathbf{k}\tilde{\phi}(\mathbf{k}) \exp[i\mathbf{k}\cdot\mathbf{x}_0]\left\{\frac{ik_x}{CB}\right\}, \tag{C6}$$

$$\omega_y = \int d\mathbf{k}\tilde{\phi}(\mathbf{k}) \exp[i\mathbf{k}\cdot\mathbf{x}_0]\left\{\frac{-(k_x^2 + k_z^2)}{B}\right\}, \quad \text{and} \tag{C7}$$

$$\partial_z w = \int d\mathbf{k}\tilde{\phi}(\mathbf{k}) \exp[i\mathbf{k}\cdot\mathbf{x}_0]\left\{\frac{-k_x k_z}{CB}\right\}. \tag{C8}$$

We define the spectrum as $\Phi_a(\mathbf{k})\delta(\mathbf{k} - \mathbf{k}') = \langle\tilde{a}^*(\mathbf{k})\tilde{a}(\mathbf{k}')\rangle$, where $\langle\ \rangle$ is the ensemble average and a is the observed variable. The response function is defined as the ratio of the measured spectrum and the true spectrum, $R_a(\mathbf{k}, l) = \Phi_a(\mathbf{k}, l)/\Phi_a(\mathbf{k})$. Response functions for velocity, vorticity, and strain spectra have the forms of

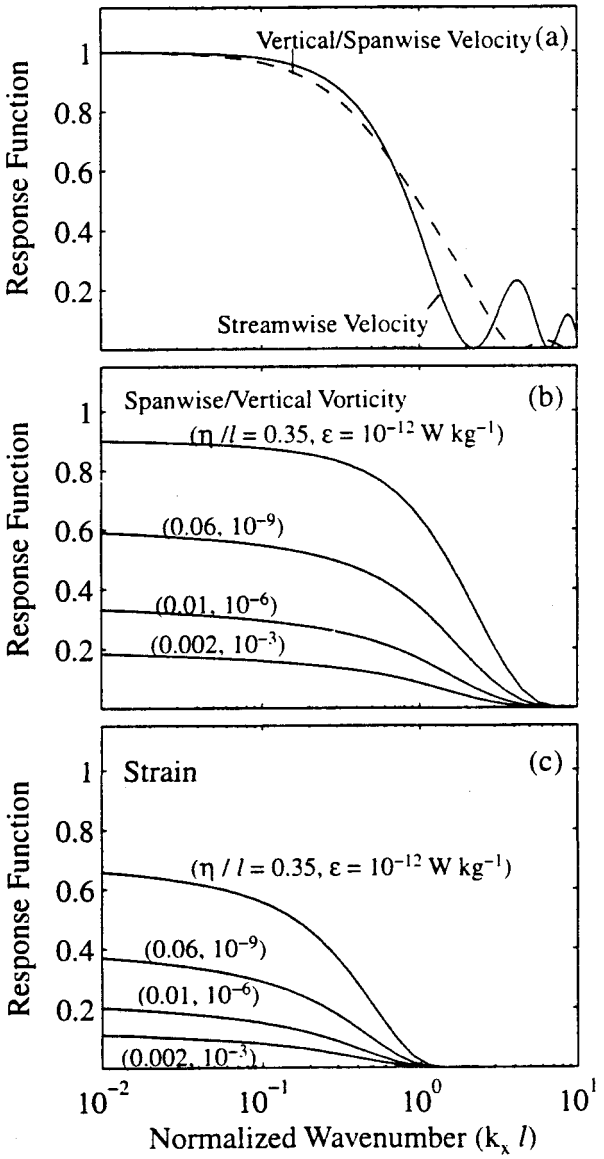

FIG. C2. One-dimensional wavenumber response function for (a) velocity, (b) vorticity, and (c) strain evaluated using Pao's spectral form. The response function for the spanwise velocity is different because the turbulent fluctuations are assumed to be advected in the streamwise direction at a speed of 0.5 m s^{-1}.

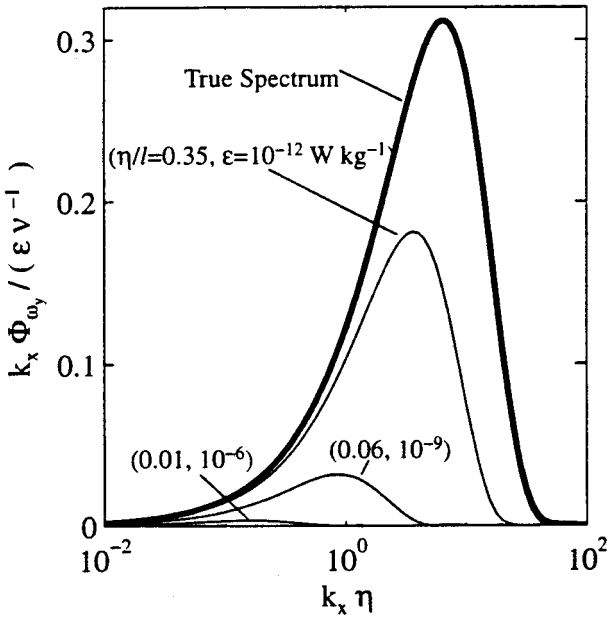

FIG. C3. Variance-preserving plot of measured vorticity (thin lines) and true vorticity (thick line). The vorticity is scaled by $\varepsilon\nu^{-1}$, and k_x is scaled by the Kolmogorov length $\nu^{3/4}\varepsilon^{-1/4}$. The sensor scale l is 8.9 cm. Only for low values of dissipation (and correspondingly large values of the Kolmogorov length scales) does the measured spectrum approach the true one.

$$R_u(\mathbf{k}, l) = \cos^2(lk_x/\sqrt{2})\ \mathrm{sinc}^2(lk_z/\sqrt{2}), \quad \text{(C9)}$$

$$R_w(\mathbf{k}, l) = \cos^2(lk_z/\sqrt{2})\ \mathrm{sinc}^2(lk_x/\sqrt{2}), \quad \text{(C10)}$$

$$R_{\omega_y}(\mathbf{k}, l) = \left[4\frac{\cos(lk_x/\sqrt{2})\cos(lk_z/\sqrt{2}) - 1}{(k_x^2 + k_z^2)l^2}\right]^2, \quad \text{(C11)}$$

$$R_{\partial_z w}(\mathbf{k}, l) = \mathrm{sinc}^2(lk_x/\sqrt{2})\ \mathrm{sinc}^2(lk_z/\sqrt{2}), \quad \text{(C12)}$$

where $\mathrm{sinc}(\lambda) = \sin(\lambda)/\lambda$ is the roman {sinc} function. The response function for the streamwise velocity is the product of a low-pass filter (the sinc function) and a cosine function. The low-pass filter results from the vertical averaging of streamwise velocity over the distance $\sqrt{2}l$ between electrodes 1 and 4 and between 2 and 3 (see Fig. 1). The cosine function is an effect of averaging the two estimated streamwise velocities. Similar arguments apply to the vertical velocity. Response functions for the spanwise vorticity and strain are low-pass filters in both the streamwise and vertical wavenumbers (Fig. C1), which exhibit k^{-4} responses.

The foregoing response functions are expressed in the 3D wavenumber domain, whereas EMVM measures only its 1D projection. In the bottom boundary layer, EMVM often measured time series while the vehicle was kept stationary in the streamwise x direction. The observed time series is equivalent to profiling in the streamwise (x) direction. Projected to 1D space, response functions for the spectra of the observed EMVM data can be expressed as

$$R_a(k_x, l) = \frac{\int dk_y \int dk_z \Phi_a(\mathbf{k}) R_a(\mathbf{k}, l)}{\int dk_y \int dk_z \Phi_a(\mathbf{k})}, \quad \text{(C13)}$$

where $a = u, w, \omega_y$, and $\partial_z w$. It is clear that the response function depends not only on the sensor configuration and scale but also on the 3D wavenumber spectra. For example, if all the spanwise vorticity variance is at scales much smaller than the sensor scale, the EMVM

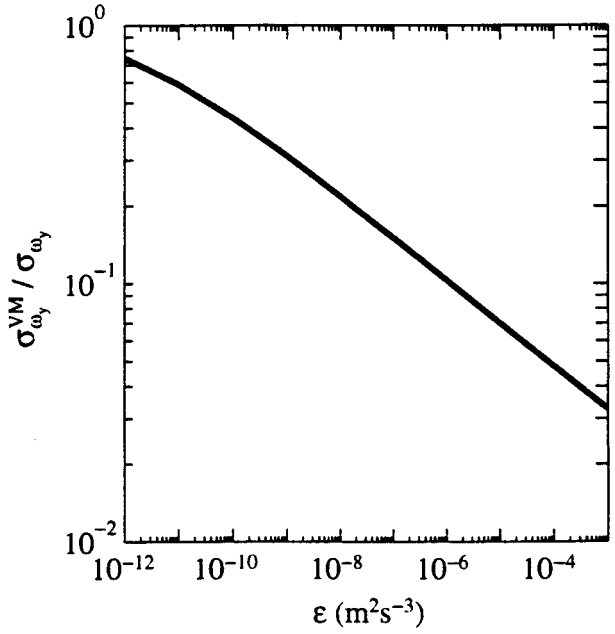

FIG. C4. The ratio of resolved and true rms spanwise vorticity as a function of ε using Pao's spectral form (see text).

will not be able to detect much of this vorticity variance at any streamwise wavenumber (k_x) (Fig. C1).

To evaluate response functions, we adopt the spectral forms for homogeneous isotropic turbulence proposed by Pao (1965), that is,

$$E(k) = \alpha \varepsilon^{2/3} k^{-5/3} \exp\left\{-\frac{3}{2}\frac{\alpha\nu}{\varepsilon^{1/3}}k^{4/3}\right\}, \quad \text{(C14)}$$

where α (=1.5) is the Kolmogorov constant (Sreenivasan 1995), ε is the kinetic energy dissipation rate, k is the 3D wavenumber, ν is the molecular viscosity, and $E(k)$ is the Kolmogorov energy spectrum. The corresponding spectra are

$$\Phi_u(\mathbf{k}) = \frac{E(k)}{4\pi k^4}(k_y^2 + k_z^2), \quad \text{(C15)}$$

$$\Phi_w(\mathbf{k}) = \frac{E(k)}{4\pi k^4}(k_x^2 + k_y^2), \quad \text{(C16)}$$

$$\Phi_{\omega_y}(\mathbf{k}) = \frac{E(k)}{4\pi k^2}(k_x^2 + k_z^2), \quad \text{and} \quad \text{(C17)}$$

$$\Phi_{\partial_z w}(\mathbf{k}) = \frac{E(k)}{4\pi k^4}k_z^2(k_x^2 + k_y^2). \quad \text{(C18)}$$

One-dimensional streamwise wavenumber spectra of velocities, vorticity, and strain are obtained by integrating over spanwise and vertical wavenumbers. The response functions expressed in (C13) are shown in Fig. C2. The response functions for the streamwise and vertical velocities are independent of ε, whereas response functions for the vorticity and vertical strain are very sensitive to it. This is because most of the vorticity variance is near the Kolmogorov length scale ($\eta = \nu^{3/4}\varepsilon^{-1/4}$), which decreases with the turbulence intensity (Fig. C3). For large ε, the sensor scale is much greater than η, and the vorticity sensor is not able fully to resolve the vorticity variance in the flow. The ratio of the resolved rms vorticity to the true rms vorticity decreases monotonically with ε, as shown in Fig. C4. Response functions for the vorticity and strain are very sensitive to the spectral distribution of $E(k)$ at high wavenumbers, where the Pao's spectrum assumed an exponential form.

REFERENCES

Baker, R. C., 1971: On the electromagnetic vortex probe. *J. Phys. E: Sci. Instrum.,* **4,** 99–101.

Bowden, K. F., 1983: *Physical Oceanography of Coastal Waters.* Ellis Horwood Ltd., 302 pp.

Briscoe, M. G., 1975: Preliminary results from the trimoored Internal Wave Experiment. *J. Geophys. Res.,* **80,** 3872–3884.

Gargett, A. E., P. J. Hendricks, T. B. Sanford, T. R. Osborn, and A. J. Williams III, 1981: A composite spectrum of vertical shear in the upper ocean. *J. Phys. Oceanogr.,* **11,** 1258–1271.

Gross, T. F., and A. R. M. Nowell, 1983: Mean flow and turbulence scaling in a tidal boundary layer. *Contin. Shelf Res.,* **2,** 109–126.

Grossman, L. M., H. Li, and H. A. Einstein, 1957: Turbulence in civil engineering: Investigations in liquid shear flow by electromagnetic induction. *Proc. Amer. Soc. Civ. Eng. J. Hydr. Div.,* 1394-1–1394-15.

Lin, J.-T., and Y.-H. Pao, 1979: Wakes in stratified fluids. *Annu. Rev. Fluid Mech.,* **11,** 317–338.

Müller, P., 1984: Small-scale vortical motions. *Internal Waves and Small-Scale Turbulence: Proc. Hawaii Winter Workshop, University of Hawaii at Manoa,* Manoa, HI, Hawaii Institute of Geophysics, 249–262.

——, G. Holloway, F. Henyey, and N. Pomphrey, 1986: Nonlinear interactions among internal gravity waves. *Rev. Geophys.,* **24,** 493–536.

Pao, Y. H., 1965: Structure of turbulent velocity and scalar fields at large wavenumbers. *Phys. Fluids,* **8,** 1063–1075.

Saffman, P. G., 1981: Dynamics of vorticity. *J. Fluid Mech.,* **106,** 49–58.

Sanford, T. B., J. A. Carlson, and M. D. Prater, 1995: An electromagnetic vorticity meter. Tech. Rep. APL-UW TR 9503, Applied Physics Laboratory, University of Washington, 140 pp. [Available from University of Washington, 1013 N.E. 40th St., Seattle, WA 98105-6698.]

Shercliff, J. A., 1962: *The Theory of Electromagnetic Flow-Measurement.* Cambridge University Press, 149 pp.

Sreenivasan, K., 1995: On the universality of the Kolmogorov constant. *Phys. Fluids,* **7,** 2778–2784.

Sternberg, R. W., 1968: Friction factors in tidal channels with differing bed roughness. *Mar. Geol.,* **6,** 243–260.

Thwaites, E. T., A. J. Williams III, E. A. Terray, and J. H. Trowbridge, 1995: A family of acoustic vorticity meters to measure ocean boundary layer shear. *Proc. IEEE Fifth Working Conf. on Current Measurement,* New York, NY, IEEE, 193–198.

Tsinober, A., E. Kit, and M. Teitel, 1987: On the relevance of the potential-difference method for turbulence measurements. *J. Fluid Mech.,* **175,** 447–461.

Wallace, J. M., and J. F. Foss, 1995: The measurement of vorticity turbulent flows. *Annu. Rev. Fluid Mech.,* **27,** 469–514.

Wyngaard, J. C., 1969: Spatial resolution of the vorticity meter and other hot-wire arrays. *J. Sci. Instrum. (J. Phys.),* **2,** 983–987.